Soft Matter

PAPER

Cite this: *Soft Matter*, 2018, **14**, 5665

Elastic capsules at liquid–liquid interfaces

Jonas Hegemann,[a] Horst-Holger Boltz [b] and Jan Kierfeld *[a]

Received 14th February 2018,
Accepted 5th June 2018

DOI: 10.1039/c8sm00316e

rsc.li/soft-matter-journal

We investigate the deformation of elastic microcapsules adsorbed at liquid–liquid interfaces. An initially spherical elastic capsule at a liquid–liquid interface undergoes circumferential stretching due to the liquid–liquid surface tension and becomes lens- or discus-shaped, depending on its bending rigidity. The resulting elastic capsule deformation is qualitatively similar, but distinct from the deformation of a liquid droplet into a liquid lens at a liquid–liquid interface. We discuss the deformed shapes of droplets and capsules adsorbed at liquid–liquid interfaces for a whole range of different surface elasticities: from droplets (only surface tension) deforming into liquid lenses, droplets with a Hookean membrane (finite stretching modulus, zero bending modulus) deforming into elastic lenses, to microcapsules (finite stretching and bending modulus) deforming into rounded elastic lenses. We calculate capsule shapes at liquid–liquid interfaces numerically using shape equations from nonlinear elastic shell theory. Finally, we present theoretical results for the contact angle (or the capsule height) and the maximal capsule curvature at the three phase contact line. These results can be used to infer information about the elastic moduli from optical measurements. During capsule deformation into a lens-like shape, surface energy of the liquid–liquid interface is converted into elastic energy of the capsule shell giving rise to an overall adsorption energy gain by deformation. Soft hollow capsules exhibit a pronounced increase of the adsorption energy as compared to filled soft particles and, thus, are attractive candidates as foam and emulsion stabilizers.

1 Introduction

Microcapsules, "hollow microparticles composed of a solid shell surrounding a core-forming space available to permanently or temporarily entrapped substances",[1] can be produced artificially and serve as container and delivery systems in many applications, or as a model for biologically relevant elastic containers, such as cells, virus capsules and red blood cells.[2–12] There are various methods to produce artificial microcapsules[4,13] resulting in solid shells composed of, for example, colloidal particles in colloidosomes,[2,14] quasi two-dimensional polymerized networks[15] and polymer multilayers,[3,4] and even bacterial films can form elastic capsules.[16] Also polyelectrolyte self-assembly in a single microfluidic production step has recently been demonstrated.[17] The core-forming space can be made from pure liquids, polymer matrices (gel-like), or solid cores.[11] All these different techniques regarding the solid shell and the core-forming space give rise to tunable elastic properties and deformation behavior.

The exact composition of the solid shell and the core-forming space depends on the specific application, where requirements might be of chemical, biological or mechanical nature. Drugs are the main application of microcapsules nowadays.[8] In medicine, microcapsules enable targeted release of incorporated drugs or cells under certain conditions.[4,5] Moreover, microcapsules are used for food,[6] textiles,[7] cosmetics,[8] self-healing materials[9,10,18] and powders.[11]

For many applications, in particular if rupture and release are involved, characterization of the mechanical properties of the capsule shell, *i.e.*, its elastic moduli, is necessary.[19,20] Elasticity protects microcapsules from breakage or rupture by converting externally applied forces into deformation energy. This enables microcapsules to resist high external loads, pass through thin capillaries, and take diverse shapes.

In this paper, we investigate elastic capsules at an interface between two liquid phases A and B, see Fig. 1. If the capsule adsorbs to an external liquid–liquid interface, this interface exerts a tensile line stress on the capsule as shown in Fig. 1(A). If two liquid phases A and B coexist inside the capsule, for example, after a phase separation process, the liquid–liquid interfaces exert a contractile line tension, see Fig. 1(B). Similar systems with contractile line tensions are liquid droplets in contact with a membrane,[21] two-component vesicles after phase separation,[22] or cells during mitosis,[23] where the tension

[a] *Physics Department, TU Dortmund University, 44221 Dortmund, Germany. E-mail: jan.kierfeld@tu-dortmund.de*
[b] *Institute for Nonlinear Dynamics, University of Göttingen, 37077 Göttingen, Germany*

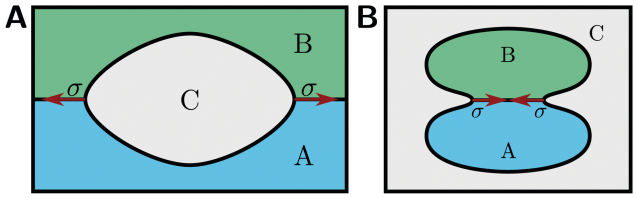

Fig. 1 (A) Capsule stretched into a lenticular shape by an interface between two liquid phases A and B outside the capsule. (B) Capsule compressed into a dumbbell shape by an interface between two liquid phases A and B inside the capsule, which can form, for example, by phase separation.

is exerted by the contractile actin ring. We will mainly focus on capsules adsorbed to liquid interfaces exerting tensile stresses in this paper, but the corresponding shapes for contractile stresses can be obtained using the same theoretical approaches provided in this paper.

There have been various studies concerning hard particles at liquid–liquid interfaces[24,25] that can be extended to deformable particles resulting in an additional degree of tunability. Recently, the spreading of filled soft particles made from crosslinked gels (microgel particles) at liquid–liquid interfaces has been investigated experimentally,[26] by molecular dynamics simulations,[27,28] and analytically.[29] When it comes to collective phenomena, experiments with microgel particles enclosing solid silica cores have revealed complex packing phenomena at the interface.[30] Interfaces with hard particles enclosing soft shells also exhibit special elasticity with constitutive relations that change upon hard core contact.[31]

Soft particles at liquid–liquid interfaces are efficient emulsifiers because they can stretch during adsorption.[29] Adsorption to the liquid–liquid interface takes place if the liquid–liquid surface tension is sufficiently high, such that there is a net energy gain from a reduction of the liquid–liquid interface area. Under these conditions, soft particles are stretched at the liquid–liquid interface and assume an energetically optimal lens-like shape,[27–29] which further increases the occupied interface area at the cost of increased elastic energy. The lower this cost, *i.e.*, the softer the particle, the greater the interface area that gets occupied, and the more the reduction in the total energy of the liquid–liquid interface by adsorbed particles.

Therefore, hollow elastic capsules with a thin elastic shell, which are much softer than filled particles, are very attractive candidates to further improve emulsification. We will characterize their deformation behavior in detail in this paper and show that elastic capsules at a liquid–liquid interface take discus- or lens-like shapes due to surface tension in the interface plane, which leads to an expansion of the capsule circumference against stretching forces and bending moments in the shell, see Fig. 2. The shape of elastic capsules resembles the well-known lens-like shapes of a liquid droplet partially wetting a liquid–liquid interface as shown in Fig. 2(A). Varying the surface tension *versus* Young's and bending moduli of the capsule we will systematically study the crossover from surface tension dominated droplet-like elasticity (liquid lens in Fig. 2(A)) to Hookean membrane elasticity for finite Young's modulus but zero bending modulus (elastic lens in Fig. 2(B)) to shell elasticity with finite Young's and bending moduli (rounded elastic lens in Fig. 2(C)).

Apart from modifying the adsorption behavior, capsule deformation by interfacial circumferential tension constitutes an independent hydrostatic method of probing the elastic properties of microcapsules. Understanding the deformation under known external loads allows for elastometry, *i.e.*, the determination of the elastic properties of the capsule's shell, which in turn can be used to infer information about the physics and chemistry of the shell, for example, its state of crosslinking.

We will show that the overall shape of the deformed capsule – the height or contact angle of its lens-like shape – allows us to infer information about the Young's modulus of the capsule shell, whereas the meridional curvature at the "tips" of the rounded lens, *i.e.*, across the interfacial plane where the tensile

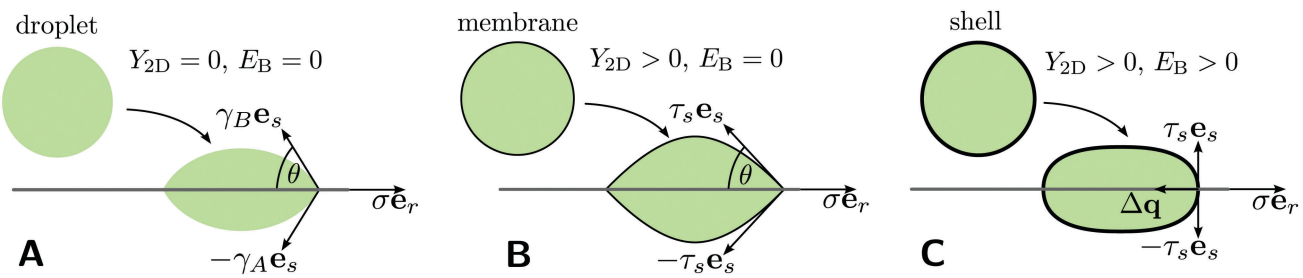

Fig. 2 Deformation following adsorption to an interface between two liquid phases (A and B in the lower and upper half-space, respectively, of the sketch depicts the symmetric case $\gamma_A = \gamma_B$) for (A) a liquid droplet, (B) a spherical membrane coated droplet, (C) a spherical shell coated droplet or microcapsule. (A) A liquid droplet deforms into a lenticular shape. Such a liquid lens consists of two spherical caps with a kink at the interface, where surface tensions are balanced in Neumann's triangle. (B) Adsorption of a thin spherical elastic capsule to a planar liquid–liquid interface yields an elastic lens, where the kink at the interface is still preserved but shapes are no longer exact spherical caps. Tangential stresses τ_s and the liquid–liquid surface tension σ acting along the liquid interface have to balance at the interface in Neumann's triangle. (C) Finally, adsorbed elastic shells exhibit a lens-like shape with a rounded edge due to a finite thickness of the material. Now, tangential stresses τ_s, liquid–liquid surface tension σ, and the discontinuity Δq in the normal transverse shear force density q have to balance each other at the contact line.

tension acts allows us to infer information about the bending modulus of the shell (if the surface tension of the liquid–liquid interface that exerts the tensile stress is known). Other static non-contact elastometry methods following the same philosophy are the study of deformations of pendant capsules under volume changes to obtain elastic moduli as investigated in ref. 32–34, the study of the edge curvature of buckled shapes to obtain the bending modulus,[35] or the study of shapes of osmotically buckled capsules to infer the osmotic pressure.[36] Non-contact techniques requiring motion in the surrounding fluid are shape analysis in shear flow,[37,38] in extensional flow,[39] and spinning drop rheometry.[40]

The paper is structured as follows: first, we discuss relevant capillary length scales and introduce our elastic model for the deformation of a microcapsule of fixed volume using shape equations. The external stretching force that the liquid–liquid interface exerts on the capsule is taken into account *via* a Neumann triangle construction for the force equilibrium at the contact line between the capsule and liquid–liquid interface. Then, we discuss numerical solutions for the resulting shapes in three elasticity regimes: the well-known droplet limit, where only surface tension acts and the capsule becomes equivalent to a droplet partially wetting the liquid–liquid interface; the membrane regime corresponding to a shell of vanishing thickness but with finite Young's modulus; and the shell regime, where we also account for bending moments and transverse shear stress due to the shell's finite thickness. We then discuss how to extract Young's and bending moduli from characteristics of deformed capsule shapes based on analytical results. Finally, we use our results on capsule deformation to calculate the enhancement of the adsorption energy for hollow capsules for decreasing shell thickness.

2 Methods

In the following, we introduce our model of a microcapsule as a Hookean shell. We start with the elastic model parameters, which also give rise to different capillary length scales controlling the deformation by the liquid–liquid surface tension and the relevance of gravitational effects. We introduce the geometric description for axisymmetric shells, the elastic energy, constitutive relations, and finally the shape equations, which can be used to obtain shape profiles by numerical integration. The shape equation approach has also been used in ref. 32, 34–36, 41 and 42. Therefore, we defer details to Appendix A. The deformation by a localized circumferential stretching force due to the liquid–liquid surface tension is the novel aspect in the present problem, which is taken into account by employing appropriate matching conditions at the three phase contact line with the liquid–liquid interface.

2.1 Elastic parameters and capillary length scales

The capsule is enclosed by an elastic shell of thickness H whose resting shape is a sphere with radius R_0. In the limit of a thin shell, $H \ll R_0$, made from an isotropic and homogeneous elastic material with Young's modulus Y_{3D}, we can use an effectively two-dimensional description with a two-dimensional Young's modulus $Y_{2D} = Y_{3D}H$ and a bending modulus given by[43]

$$E_B = \frac{Y_{2D}H^2}{12(1-\nu_{2D}{}^2)}, \tag{1}$$

where ν_{2D} is the two-dimensional Poisson ratio. Choosing R_0 as unit of length and Y_{2D} as unit of tension, the dimensionless bending modulus is given by

$$\tilde{E}_B = \frac{E_B}{Y_{2D}R_0{}^2} = \frac{1}{\gamma_{FvK}} = \frac{1}{12(1-\nu_{2D}{}^2)}\frac{H^2}{R_0{}^2}, \tag{2}$$

where γ_{FvK} is the Föppl–von-Kármán number, and the last equality again assumes (cp. eqn (1)) a thin shell made from an isotropic and homogeneous elastic material. Note that we use the same units throughout the paper, *i.e.*, we measure tensions in units of the Young's modulus Y_{2D} and lengths in units of the resting shape's radius R_0. Using these natural units we transform quantities x to their dimensionless counterparts $\tilde{x}$.

By fixing the Poisson ratio $\nu_{2D} = 1/2$ (corresponding to a linearly incompressible bulk material) the capsule's elastic response to external forces is solely determined by the dimensionless bending modulus $\tilde{E}_B$. Typical values for microcapsules range within $\tilde{E}_B = 10^{-10}\ldots10^{-1}$ assuming $E_B = 10^{-16}\ldots10^{-14}$ N m, $Y_{2D} = 10^{-2}\ldots10$ N m^{-1} and $R_0 = 10^{-6}\ldots10^{-3}$ m.[34] If $\tilde{E}_B \sim 10$ (corresponding to $H \sim R_0$ for $\nu_{2D} = 1/2$) we expect to obtain (at least qualitatively) the crossover to the limit of a filled soft particle that has been considered in ref. 27–29.

Based on Young's modulus we can estimate the typical deformation. The capsule will be stretched by the surface tension σ of the liquid–liquid interface, which acts along the circumference of the capsule. A deformation by ΔR at the liquid–liquid interface causes strains $\sim\Delta R/R_0$ and costs an elastic stretching energy $E_{el} \sim Y_{2D}R_0{}^2(\Delta R/R_0)^2 \sim Y_{3D}HR_0{}^2(\Delta R/R_0)^2$ but gains an interfacial energy $E_\sigma \sim \sigma R_0\Delta R$. The resulting strain is of order $\Delta R/R_0 \sim \sigma/Y_{2D} \sim \sigma/Y_{3D}H$, *i.e.*, independent of capsule size but limited by shell thickness for hollow capsules. The behavior is different for a filled soft particle, where we expect $\Delta R/R_0 \sim \sigma/Y_{3D}R_0$, *i.e.*, small filled particles deform stronger than large filled particles. For filled soft particles, this allows to define an elastocapillary length $L_\sigma = \sigma/Y_{3D}$ such that deformations by the surface tension σ become large for small particles $R_0 \ll L_\sigma$.[29,44] For hollow capsules with a soft shell, on the other hand, deformations become large if the shell thickness H is sufficiently small compared to the elastocapillary length: $H \ll L_\sigma$ (or $\sigma \gg Y_{2D}$). We can generally state that hollow capsules deform more significantly than filled soft particles of the same size.

Although the size of the capsule is not relevant for deformation by the liquid–liquid interface, it will play a role in deformation by gravitational forces. The typical gravitational energy gain upon deformation by ΔR is $E_g \sim \Delta\rho g R_0{}^3\Delta R$, where $\Delta\rho$ is the density difference between the liquids inside

and outside the capsule. Gravitational energy competes with the elastic deformation energy E_{el} resulting in strains $\Delta R/R_0 \sim \Delta\rho g {R_0}^2/Y_{2D}$, *i.e.*, deformation by gravitation is relevant for capsules larger than a gravitational elastocapillary length $L_g = (Y_{2D}/\Delta\rho g)^{1/2}$.

Moreover, capsule size is also relevant for the deformation of the liquid–liquid interface by the gravitational force on the capsule, *i.e.*, the shape of the meniscus. The balance of the gravitational energy E_g and the interfacial energy E_σ shows that the meniscus is curved on the scale of the capillary length $L_c = (\sigma/\Delta\rho g)^{1/2}$. Only capsules larger than L_c give rise to a relevant curvature of the liquid–liquid interface.[44]

We will focus on soft hollow capsules with $H \ll R_0$, for which gravitational effects both for the meniscus and capsule deformation are negligible, *i.e.*, $R_0 \ll L_g$, L_c, and strains of the capsule do not become large but are non-negligible, *i.e.*, $H \geq L_\sigma$ or $\sigma \leq Y_{2D}$. For artificial microcapsules this is a generic situation, as the following estimates show: for microcapsules with $R_0 \sim 10$ μm with a typical soft capsule shell material with $Y_{2D} \sim 10^{-2}\ldots10^{-1}$ N m^{-1} and a shell thickness $H \sim 0.1$ μm (corresponding to $Y_{3D} = Y_{2D}/H \sim 10^5\ldots10^6$ Pa), with a liquid–liquid interfacial tension (*e.g.* oil–water) of $\sigma \sim 5 \times 10^{-2}$ N m^{-1}, and with $\Delta\rho \sim 10^2$ kg m^{-3}, we find a capillary length $L_c \sim 7$ mm and a gravitational elastocapillary length $L_g \sim 3\ldots10$ mm, which are much larger than R_0, and an elastocapillary length $L_\sigma \sim 5 \times 10^{-2}\ldots10^{-1}$ μm, which is of the order of the thickness H.

2.2 Parametrization

We consider the axisymmetric elastic shell as a surface of revolution around the z-axis (see Fig. 7 in the Appendix for details). The shell contour (its generatrix) is given in cylindrical coordinates $(r(s_0), z(s_0))$, where s_0 is the arc length of the undeformed shape and r is the distance from the z-axis. The total arc length of the contour is L_0, *i.e.*, $s_0 \in [0,L_0]$. The arc length element of the deformed shape derives as $\mathrm{d}s = \sqrt{r'(s_0)^2 + z'(s_0)^2}\mathrm{d}s_0$, and the unit tangent vector $\vec{e}_s = (\cos\psi, \sin\psi)$ (ψ being the angle between $\vec{e}_s$ and the r-axis) gives the orientation of a capsule patch relative to the axis of symmetry. The undeformed reference shape shall be given by a sphere with rest radius R_0, *i.e.*, $(r_0(s_0), z_0(s_0)) = (R_0 \sin(\pi s_0/L_0), z_0 + R_0(1 - \cos(\pi s_0/L_0)))$, which generates (by revolution around the z-axis) a sphere with radius R_0 whose lower apex (intersection with the symmetry axis) is located at z_0 and $s_0 = 0$.

2.3 Elastic energy

Stretching deformations with respect to the undeformed spherical shape can be expressed in terms of the stretches $\lambda_s = \mathrm{d}s/\mathrm{d}s_0$ and $\lambda_\phi = r/r_0$, and bending deformations in terms of the principal curvatures $\kappa_s = \mathrm{d}\psi/\mathrm{d}s$ and $\kappa_\phi = \sin\psi/r$, which derive from the second fundamental form of a surface of revolution.[45] The deformation energy is formulated best in terms of the (stretching) strains $e_{s,\phi} = ({\lambda_{s,\phi}}^2 - 1)/2 \approx \lambda_{s,\phi} - 1$ employing a small strain approximation and bending strains $K_{s,\phi} = \lambda_{s,\phi}\kappa_{s,\phi} - \kappa_{s_0,\phi_0}$, where we expanded up to linear order in deviations from the undeformed reference shape with $\lambda_s = \lambda_\phi = 1$ and $\kappa_{s,\phi} = \kappa_{s_0,\phi_0}$.† We consider hyperelastic materials, whose elastic energy can be expressed in terms of a local energy density, and use a Hookean surface energy density[43]

$$w(s_0)\mathrm{d}A_0 = \frac{1}{2}\Big(\frac{Y_{2D}}{(1-{\nu_{2D}}^2)}\big({e_s}^2 + 2\nu_{2D}e_s e_\phi + {e_\phi}^2\big) + E_B\big({K_s}^2 + 2\nu_{2D}K_sK_\phi + {K_\phi}^2\big) + \lambda_s\lambda_\phi\gamma\Big)\mathrm{d}A_0 \quad (3)$$

with the linear approximation $e_{s,\phi} \approx \lambda_{s,\phi} - 1$. The three terms in the energy density correspond to the three contributions from stretching, from bending, and from an effective interfacial tension between the fluids outside and inside the capsule. We consider capsules smaller than the gravitational elastocapillary length L_g, thus we can neglect gravitational body forces in the energy. We explicitly state the undeformed surface element $\mathrm{d}A_0$ to highlight the fact that this energy functional operates on the undeformed surface which is important for computing stresses from it.

The energy (3) explicitly contains a contribution from an isotropic effective surface tension γ between the outer liquids and the capsule. Such a contribution arises either as the sum of surface tensions of the liquid outside with the outer capsule surface and the liquid inside with the inner capsule surface or, if the capsule shell is porous such that there is still contact between the liquids outside and inside the capsule, with additional contributions from the surface tension between outside and inside liquids. In general, the liquid phases A in the lower half-space and B in the upper half-space will have different surface tensions $\gamma = \gamma_A$ and $\gamma = \gamma_B$ with the capsule. We will distinguish between the simpler symmetric case $\gamma_A = \gamma_B$ (which is also depicted in Fig. 2) and the general asymmetric case with $\gamma_A \neq \gamma_B$. We will mainly focus on the symmetric case throughout the paper, where the AB-interface acts along the equator of the capsule.

The dimensionless surface tension γ/Y_{2D} (with $\gamma \equiv \gamma_A = \gamma_B$ in the symmetric case) is another important control parameter of the capsule, which governs the crossover from a liquid droplet to an elastic Hookean membrane or shell: for $\gamma/Y_{2D} \gg 1$ the capsule behaves as a liquid droplet and assumes a lens-like shape as in Fig. 2(A). For $\gamma/Y_{2D} \ll 1$ the capsule behaves either as a Hookean membrane also assuming a lens shape as in Fig. 2(B) (for small bending moduli $\tilde{E}_B$) or as an elastic shell assuming a rounded lens shape as in Fig. 2(C) (for larger bending moduli $\tilde{E}_B$).

† Systematic derivations starting from thin three-dimensional elastic materials[46,47] show that factors $\lambda_{s,\phi}$ should be contained in the definition of bending strains. As a result, a spherical shell that is uniformly stretched from radius R_0 to radius R has $\lambda_{s,\phi} = R/R_0$ and $\kappa_{s,\phi} = 1/R \neq \kappa_{s_0,\phi_0} = 1/R_0$ but vanishing $K_{s,\phi} = 0$, which is reasonable because it has obviously not developed bending moments but only stretching tensions. For strictly two-dimensional materials with bending energy functionals such as the Helfrich energy, the curvature cannot be changed by stretching the material.

We assume a spherical rest shape of the capsule, *i.e.*, the capsule is not synthesized at the liquid–liquid interface but inside one of the liquid phases A or B before it is adsorbed to the interface. As already worked out in ref. 29, adsorption of a spherical particle to the AB-interface also depends on the surface tension σ of the AB-interface: If $\gamma_A > \gamma_B + \sigma$ the particle stays in liquid B, if $\gamma_B > \gamma_A + \sigma$ the particle stays in liquid A. For sufficiently large $\sigma > |\gamma_A - \gamma_B|$, the particle will always adsorb to the interface.

We note that the energy functional (3) (with $\nu_{2D} = 1/2$) also correctly describes the low-strain behavior of more sophisticated energy functionals, *e.g.*, of the Mooney–Rivlin type.[43,48] In this regard, our model as well as the constitutive relations given below are a small strain limit. The Hookean small strain description is often sufficient and the most simple though a non-trivial choice. For larger strains, Mooney–Rivlin, Skalak or other elastic energies are more appropriate. In general, we expect large strains to occur for stretching tensions $\sigma > Y_{2D}$ ($H < L_\sigma$) and $\sigma > \gamma$. Tensile stresses $\sigma \leq Y_{2D}$ are realistic for typical experimental situations. In Appendix A.1, we find that, for $\sigma \leq Y_{2D}$, meridional strains remain small, whereas circumferential stretching factors can become locally large, where the liquid–liquid tension acts (reaching values $\lambda_\phi \simeq 1.8$ for $\sigma = Y_{2D}$, see Fig. 8 in the Appendix). We do not expect, however, that any of our results will qualitatively change if nonlinear elastic laws beyond Hookean elasticity are used in this regime. This is also what has been found for deflated pending capsule shapes in ref. 34.

2.4 Constitutive relations

Variation of the elastic energy with respect to the strains $e_{s,\phi}$ gives the tensions $\tau_{s,\phi}$; variation with respect to the curvatures $K_{s,\phi}$ gives the bending moments $m_{s,\phi}$. This gives the corresponding constitutive relations of the capsule material for a Hookean elastic material,

$$\begin{aligned} \tau_{s,\phi} &= \frac{1}{\lambda_{\phi,s}}\frac{\partial w}{\partial e_{s,\phi}} = \frac{Y_{2D}}{1-{\nu_{2D}}^2}\frac{1}{\lambda_{\phi,s}}\left(e_{s,\phi} + \nu_{2D} e_{\phi,s}\right) + \gamma, \\ m_{s,\phi} &= \frac{1}{\lambda_{\phi,s}}\frac{\partial w}{\partial K_{s,\phi}} = \frac{E_B}{\lambda_{\phi,s}}\left(K_{s,\phi} + \nu_{2D} K_{\phi,s}\right), \end{aligned} \tag{4}$$

which are nonlinear since the Cauchy stresses are defined with respect to the deformed arc length, but the surface energy density measures lengths in terms of the undeformed arc length. Note that the surface tension γ gives a constant and isotropic contribution to the tensions τ_s and τ_ϕ.

2.5 Shape equations

The equilibrium shape of an infinitesimal thin shell is described by local stress equilibrium in tangential and normal directions; elastic shells of finite thickness additionally require torque (bending moment) balance (see Appendix A.1). In combination with the constitutive laws (4) and three differential equations following from cylindrical parametrization the stress and moment equilibrium lead to a closed system of six shape equations for axisymmetric Hookean shells,

$$\begin{aligned} r'(s_0) &= \lambda_s \cos\psi, \quad z'(s_0) = \lambda_s \sin\psi, \quad \psi'(s_0) = \lambda_s \kappa_s, \\ {\tau_s}'(s_0) &= \lambda_s\left(\frac{\tau_\phi - \tau_s}{r}\cos\psi + \kappa_s q + p_s\right), \\ {m_s}'(s_0) &= \lambda_s\left(\frac{m_\phi - m_s}{r}\cos\psi - q\right), \\ q'(s_0) &= \lambda_s\left(-\kappa_s \tau_s - \kappa_\phi \tau_\phi - \frac{q}{r}\cos\psi + p\right), \end{aligned} \tag{5}$$

where the quantity q is the transverse shear stress, $p = p_0 + p_n$ is the total internal normal pressure, and p_s is the shear pressure. Since we consider a closed microcapsule encapsulating an incompressible liquid phase, p will have a hydrostatic contribution, p_0, that has to be fixed by the volume constraint (see Appendix A.1). Throughout the paper we consider closed microcapsules containing an incompressible liquid phase. Therefore, all deformations are at fixed volume, which is given by $V = 4\pi {R_0}^3/3$ for an elastic capsule with a spherical rest shape of radius R_0. External forces from the surface tension σ of the AB-interface enter *via* the additional normal and shear pressures p_n and p_s and will be discussed in the following section in detail. We consider capsules smaller than the gravitational elastocapillary length L_g, such that we can neglect a gravitational contribution $-\Delta\rho g z$ to the pressure p in the last shape equation, see also Section 2.7 below.

The first three equations in (5) are geometric relations. The fourth and sixth equations in (5) describe the tangential and normal force equilibrium, respectively. The fifth equation is the equilibrium of bending moments. Equivalently, the fourth and fifth shape equations in (5) can be obtained by a variational approach, where we minimize the total free energy

$$G = \int w(s_0)\mathrm{d}A_0 - p_0 V + E_\sigma \tag{6}$$

with respect to the independent functions $r(s_0)$ and $\psi(s_0)$ (we repeat this calculation from ref. 35 in Appendix A.1.1 for completeness of the presentation) and where E_σ is the potential energy for the external forces from the surface tension σ (see following section). The sixth shape equation in (5) is equivalent to an additional algebraic relation $q = -\tau_s \tan\psi + pr/2\cos\psi$ (see also eqn (38) in Appendix A.2), which is obtained in this variational calculation. The shape eqn (5) are closed by eliminating λ_s and τ_ϕ by using the two constitutive relations for stresses and strains from eqn (4), using the geometric relation $\kappa_\phi = \sin\psi/r$, and eliminating κ_s and m_ϕ by using the two constitutive relations for bending moments and bending strains from eqn (4). This procedure is explained in detail in ref. 35.

The shape equations in the form (5) are still independent of the elastic material law and only contain stress and moment equilibrium and geometrical relations but no information on the elastic material law, *i.e.*, the constitutive relation. The constitutive relation is needed to close the shape equations. We use the nonlinear Hookean elasticity (4) but also other

constitutive relations can be implemented. In ref. 34 it has been explicitly shown how to use a Mooney–Rivlin relation to close the shape eqn (5).

Because the six shape eqn (5) are of first order, six boundary conditions are needed. Boundary conditions at the apices ($s_0 = 0$ and $s_0 = L_0$) are $r(0) = r(L_0) = 0$ because the capsule is closed, $\psi(0) = \pi - \psi(L_0) = 0$ because there are no kinks, and $q(0) = q(L_0) = 0$ because there are no point loads at the apices which could cause a transverse shear stress q. The boundary conditions to the remaining quantities z, τ_s, and m_s are *a priori* unknown, and we have to solve the shape eqn (5) by a shooting method as explained in Appendix A.3 to fulfill boundary conditions at both apices.

2.6 Matching conditions at the liquid–liquid interface

The aim of this paper is to study the deformation behavior of microcapsules during adsorption at a planar liquid–liquid interface, which can be found, for example, between two horizontally layered immiscible liquids A and B. We assume the AB-interface to be in the horizontal plane at $z = 0$ and define the corresponding arc length $s_0 = \ell$ by $z(\ell) = 0$. Gravity can lead to a lowering of the adsorbed capsule, which will deform the AB-interface.[44] We focus on capsules smaller than the capillary length $R_0 \ll L_c$ such that this effect can be neglected. We will only briefly discuss gravity effects in more detail in the next Section 2.7. Neglecting gravity we have a purely horizontal stretching force from the interfacial tension σ from the AB-interface. We will refer to σ as the interface load because σ is responsible for stretching the capsule.

Adsorption of an object that forms a circular cross-section with the horizontal interface changes the interfacial surface energy by $E_\sigma = -\sigma\pi r^2(\ell)$. From this energy we derive the force density from the interface load by variation with respect to shape changes,

$$\vec{f}_\sigma(s_0) = \sigma\delta(s_0 - \ell)\vec{e}_r, \tag{7}$$

which acts normal to the contact line of the capsule at $z = 0$ ($z(s_0 = \ell) = 0$) in the horizontal direction. The force density (7) can be formally incorporated into the shape eqn (5) as additional normal and shear pressure contributions p_n and p_s (see eqn (31) in Appendix A.1), which cannot be integrated over directly as they are singular. Instead, we can also solve (5) piecewise for $z > 0$ and $z < 0$ (corresponding to $s_0 < \ell$ and $s_0 > \ell$), and derive matching conditions at the three phase contact line at $z = 0$ or $s_0 = \ell$ to account for the force density (7).

Because the shape eqn (5) are first order, the number of matching conditions has to equal the number n of shape eqn (5) if the interface position $s = \ell$ along the capsule is known. In the symmetric case $\gamma_A = \gamma_B$, upper and lower parts of the capsule are related by reflection symmetry. Then, the AB-interface is located at the known arc length $s_0 = L_0/2$, such that n matching conditions are required. In the general asymmetric case of the AB-interface, also ℓ has to be determined, such that $n + 1$ matching conditions are required.

We first discuss the symmetric case. For a Hookean shell, we have the full set of $n = 6$ shape eqn (5). The shell becomes an elastic membrane in the limit of vanishing $H \approx 0$, *i.e.*, vanishing bending modulus $E_B \approx 0$, which implies vanishing bending moments $m_s = 0$ and vanishing transverse shear stress $q = 0$, such that only $n = 4$ shape equations are left. A liquid droplet cannot support elastic stresses, such that $Y_{2D} \approx 0$, there is no reference shape, such that $\lambda_s = \lambda_\phi = 1$, and also tangential stresses $\tau_s = \tau_\phi = \gamma$ can be eliminated from (5), leading to $n = 3$ equations equivalent to the well-known Laplace–Young shape equations, see eqn (46) in the Appendix.

In the symmetric case, we need n matching conditions to fit piecewise solutions for the upper and lower halves uniquely together. First, we have to impose continuity for the variables r and z, which ensures a closed capsule shape. In addition, we impose $z = 0$ at the interface resulting in three matching conditions.

The remaining matching conditions are derived in Appendix A.2 from variation of the total free energy (6). We find two matching conditions (40) and (41) corresponding to the balance of interfacial forces in the z- and r-direction at the three phase contact line, *i.e.*, a Neumann triangle construction[49] (see also Fig. 2). Only force balance in the r-direction involves the interfacial force (7) in the absence of gravity effects. In variational calculus the force balance equation in the r-direction is obtained as a Weierstrass–Erdmann condition from variation with respect to r. In the z-direction, the interfacial forces from the upper and lower parts of the capsule not only balance each other at the AB-interface in the Neumann construction, but each of them is also balanced by the pressure force $p_0 r/2$ because both the upper and lower parts of the capsule must be force-free in the z-direction in equilibrium (see eqn (39) in the Appendix). Therefore, continuity of the variable r is actually equivalent to the Neumann matching condition (40) in the z-direction. If both conditions are used, the set of matching conditions becomes over-determined. Interestingly, using both equations in an over-determined set of matching conditions makes our numerical analysis typically more stable.

For the Hookean membrane, two continuity conditions for r and z, the value $z = 0$ at the AB-interface, and the Neumann triangle condition (41) in the r-direction are the required $n = 4$ matching conditions to make the problem well-posed. For the Hookean shell we also get a continuity condition for ψ ensuring a smooth shape without kinks (which are forbidden by bending energy) and obtain an additional moment equilibrium (42) at the contact line (as a Weierstrass–Erdmann condition from variation with respect to ψ) resulting in the required $n = 6$ conditions for the Hookean shell.

In the general asymmetric case, the AB-interface is located at an arc length $s_0 = \ell$ ($z(\ell) = 0$), which has also to be determined from variation of the total free energy. In Appendix A.2 we find an additional transversality condition (43) by equating the boundary terms $\propto \delta\ell$ in variational calculus. This condition is equivalent to the statement that the discontinuity of the surface energy density w originates only from the discontinuity of the surface tension with the surrounding liquid γ, which jumps from γ_A to γ_B at the AB-interface. This, in turn, is equivalent to requiring that the elastic contributions to the meridional

tension $\tau_s - \gamma$ are continuous at the AB-interface (*i.e.*, their absolute values are continuous, their directions can be discontinuous, for example, in the Hookean membrane case in an elastic lens, see Fig. 2(B)).

2.7 Gravity

Body forces, such as gravitation and buoyancy, that act upon the capsule can bend the AB-interface[44] and can deform the capsule. We already showed that gravity leads to a curved meniscus of the AB-interface if the capsule radius R_0 is larger than the capillary length $L_c = (\sigma/\Delta\rho g)^{1/2}$ and that gravity deforms the capsule if the capsule radius R_0 is larger than the gravitational elastocapillary length $L_g = (Y_{2D}/\Delta\rho g)^{1/2}$. Both capillary lengths are typically of the order of millimeters, such that gravity can be neglected for microcapsules. Now we want to briefly address in more detail, how our model had to be modified in order to include all gravity effects. The involved quantities are explained in Fig. 3.

For an axisymmetric capsule the total body force containing gravitational and buoyancy force is directed in the z-direction. The AB-interface contacts the capsule at $s_0 = \ell$ but if this interface bends downward we no longer have $z(\ell) = 0$ as without gravity but $z(\ell) = -h_m$ with a height $h_m > 0$ of the meniscus (if $z = 0$ is the position of the AB-interface at infinity, see below). The buoyancy force is given by the weight difference of the volume $\pi r(\ell)^2 h_m - (V_B - V_>)$ (red area in Fig. 3) of liquid A that has been displaced by liquid B vertically above the contact line up to the original horizontal AB-interface at $z = 0$,[50] where $V_>$ is the capsule volume above the $z = 0$ plane (blue area in Fig. 3; $V_> = 0$ if the entrie capsule is below the $z = 0$ plane). The other contribution to the buoyancy force is given by the weight difference in volume $V_A + V_B - V_>$ (green area in Fig. 3) of liquid A and $V_>$ (blue area) of liquid B that have been displaced by the capsule interior C. Both contributions add up to

$$\vec{f}_{body} = [g(\rho_A - 2\rho_C)V + g(\rho_A - \rho_B)(\pi r(\ell)^2 h_m - V_B)]\vec{e}_z. \quad (8)$$

If $h_m > 0$ and the AB-interface bends, the interface load $\vec{f}_\sigma$, see eqn (7), also has a component in the $\vec{e}_z$ direction, which, integrated along the circular cross-section, exactly compensates for $\vec{f}_{body}$ in equilibrium,

$$\vec{f}_{body} + \sigma \sin(\vartheta) 2\pi r(\ell)\vec{e}_z = 0. \quad (9)$$

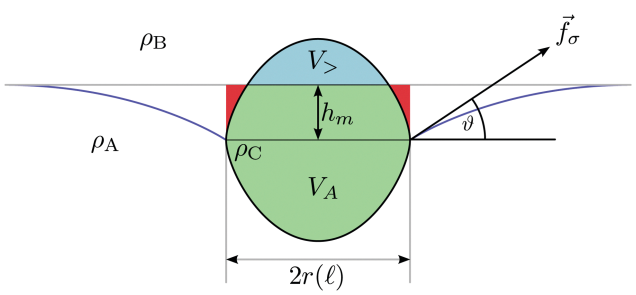

Fig. 3 Elastic capsule subjected to gravitational forces at a liquid–liquid interface. The total body force $\vec{f}_{body}$ (see eqn (8)) acting on the capsule volume is compensated for by the vertical component of the interface load $\vec{f}_\sigma$ (see eqn (7)) (integrated along the circular three phase contact line).

This determines the angle ϑ between the interface tangent and the r-axis at the three phase contact line.

If ϑ is known, the complete shape $z_{AB}(x,y)$ of the AB-interface follows from the Laplace equation, which can be written in the form

$$-\vec{\nabla} \cdot \vec{n} = \frac{z_{AB}}{L_c^2} \quad (10)$$

with a capillary length $L_c = (\sigma/\Delta\rho_{AB} g)^{1/2}$, which is determined by the density difference $\Delta\rho_{AB} = \rho_A - \rho_B$ of the two liquid phases, and with the unit normal vector $\vec{n}$ onto the AB-interface.[51] We consider the case of equal pressures in phases A and B in eqn (10) such that the interface becomes planar at infinity; we choose the z-coordinates such that the AB-interface is at $z = 0$ at infinity.

Moreover, the shape of the capsule changes in the presence of gravity. First, gravity gives rise to a hydrostatic pressure contribution $\Delta\rho g z$ to the pressure p in the last shape equation in (5), where $\Delta\rho = \Delta\rho_{AC} = \rho_A - \rho_C$ is the density difference between the capsule interior C and the liquid phase A for $s_0 < \ell$ (where the capsule is in contact with liquid A) and $\Delta\rho = \Delta\rho_{BC} = \rho_B - \rho_C$ the density difference between liquid phase B and capsule interior C for $s_0 > \ell$ (where the capsule is in contact with liquid B). Second, the matching conditions at the AB-interface have to be modified if the angle ϑ is non-zero. Then the force density $\vec{f}_\sigma = \sigma(\sin\vartheta\vec{e}_z + \cos\vartheta\vec{e}_r)$ acquires a non-zero z-component $\sigma\sin\vartheta$, which enters the Neumann triangle condition in the z-direction, and the modified r-component $\sigma\cos\vartheta$ enters the Neumann triangle condition in the r-direction.

Thus, our model can be easily extended to include all gravitational effects properly if larger, millimeter-sized capsules are considered that are no longer small as compared to the capillary length L_c or the gravitational elastocapillary length L_g.

3 Results

In the remainder of this paper, we present and discuss numerical, quantitative results from solving the shape equations for different control parameters: the dimensionless bending modulus $\tilde{E}_B$ or Föppl–von-Kármán number controlling the relevance of bending energy, the dimensionless surface tension $\tilde{\gamma} \equiv \gamma/Y_{2D}$ controlling the capsule elasticity from liquid droplet to elastic capsule, and the dimensionless interface load $\tilde{\sigma} \equiv \sigma/Y_{2D} = L_\sigma/H$ or $\tilde{\sigma}/\tilde{\gamma} = \sigma/\gamma$ characterizing the strength of the deforming force from the AB-interface. We will neglect gravitational effects, *i.e.*, consider the typical situation that microcapsules are smaller than both gravitational capillary lengths, $R_0 \ll L_g$ and $R_0 \ll L_c$.

We also discuss analytical results for characteristics of the lens-like droplet or capsule shapes, where it is possible. We will show that the height or contact angle of the lens is directly related to the Young's modulus of the capsule shell (or the surface tension of a droplet), *i.e.*, the dimensionless parameters σ/γ characterizing the tensile force exerted by the AB-interface and the dimensionless surface tension γ/Y_{2D} governing the

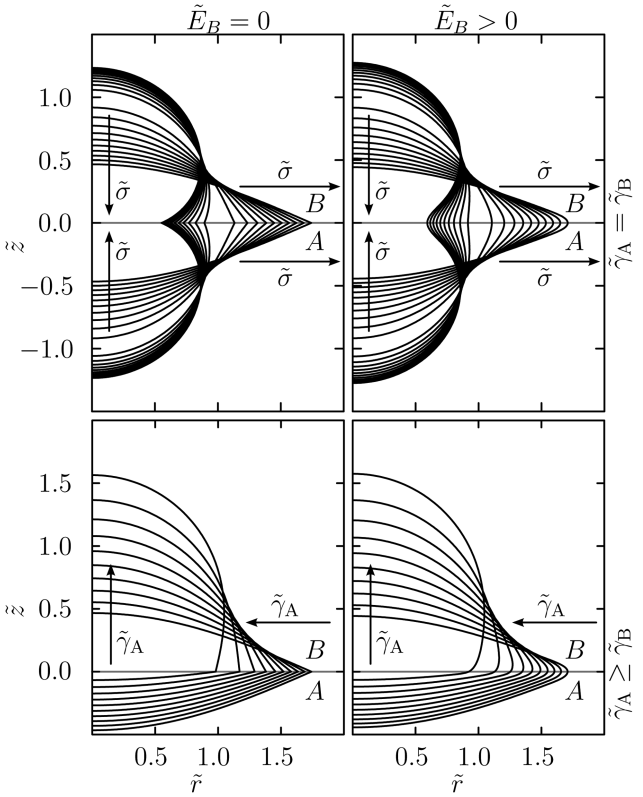

Fig. 4 Shape evolutions for the Hookean membrane ($\tilde{E}_B = E_B/Y_{2D}R_0^2 = 0$, left) and the shell ($\tilde{E}_B = 10^{-3}$, right) both for the symmetric case (upper row) and the asymmetric case (lower row). In the upper row we increase the interface load from $\tilde{\sigma} = \sigma/Y_{2D} = -1$ (contractile, dumbbell-shaped) to $\tilde{\sigma} = 1$ (extensile, discus-shaped) at a constant ratio $\gamma_A/\gamma_B = 1$ (symmetric case). In the lower row we increase the ratio of surface tensions γ_A at the A–C interface (lower half-space) and γ_B at the B–C interface (upper half-space) from $\gamma_A/\gamma_B = 1$ to $\gamma_A/\gamma_B = 10$ at a constant interface load $\tilde{\sigma} = 1$. In contrast to the Hookean shell (right), which shows a smooth and rounded edge at the interface, the Hookean membrane (left) exhibits a sharp kink at the interface due to a vanishing shell thickness. Apart from this feature, shapes look rather similar at small values of the dimensionless bending modulus $\tilde{E}_B$.

crossover from a liquid droplet to an elastic Hookean membrane or shell. The maximal curvature at the "tips" of the rounded lens allows us to infer information about the bending modulus of the shell.

Finally, we can quantify the adsorption energy gain by deformation relative to the adsorption energy gain of a hard undeformable particle, which is an important quantity for applications of capsules as surface active agents, for example, in emulsification.

In Fig. 4, we show numerically calculated evolutions of capsule shapes for varying interface loads σ, both for tensile ($\sigma > 0$) and contractile ($\sigma < 0$) tensions. We show these evolutions both for symmetric ($\gamma_A = \gamma_B$) and asymmetric surface tension between the capsule and phases A and B and both for a Hookean membrane without bending rigidity and an elastic shell ($\tilde{E}_B = 10^{-3}$). We clearly see the typical lens- or discus-like shapes for tensile interface loads. For contractile loads, a stable shape can only be obtained in the symmetric case, where we observe characteristic dumbbell shapes.

In the following paragraphs, we discuss aspects of the lens-like shapes under tensile interface loads σ quantitatively. We focus on symmetric surface tensions $\gamma_A = \gamma_B = \gamma$ (shapes in the upper part of Fig. 4) and vary the dimensionless surface tension γ/Y_{2D} and bending modulus $\tilde{E}_B$ to cover all different surface elasticities: the well-known liquid lenses for droplets partially wetting the AB-interface ($\gamma/Y_{2D} \to \infty$, $\tilde{E}_B = 0$), elastic lenses for Hookean membranes (γ/Y_{2D} finite, $\tilde{E}_B = 0$), and rounded elastic lenses for microcapsules with Hookean shell elasticity (γ/Y_{2D} finite, $\tilde{E}_B > 0$).

3.1 Droplets and membranes: lenticular shapes

In the droplet regime (vanishing elastic moduli Y_{2D} and E_B), the correct shape is found from the Laplace–Young equation, according to which the shape is assembled from spherical caps (shapes of constant mean curvature). For spherical caps the contact angle (between the tangent to the surface and the horizontal liquid–liquid interface) is related to their radius R and height h by

$$\cos\theta(\tilde{h}) = 1 - \frac{\tilde{h}}{\tilde{R}(\tilde{h})} = 2\frac{1-\tilde{h}^3}{2+\tilde{h}^3}. \tag{11}$$

Dimensionless lengths denoted with a tilde are measured in units of R_0. The dimensionless height $\tilde{h}$ of the spherical cap is its maximal distance from the circular base of the cap. For incompressible liquids as investigated in this paper the radius $\tilde{R}$ is related to the height $\tilde{h}$ of the spherical cap by the volume constraint (see eqn (53) in the Appendix), which gives the last equality in eqn (11). Balancing tensions at the three phase contact point, according to the Neumann triangle condition (41) for force balance in the r-direction, $\sigma = 2\gamma\cos\theta$, we finally find that the height $\tilde{h}$ is given by

$$\tilde{h} = \frac{2^{1/3}(2-\sigma/\gamma)^{1/3}}{(4+\sigma/\gamma)^{1/3}} \tag{12}$$

for the liquid lens (see also eqn (54) and its derivation in the Appendix). For increasing the dimensionless interface load σ/γ, the height of the liquid lens decreases until we reach the transition to complete wetting for $\sigma = 2\gamma$, where $\tilde{h} = 0$ and the liquid lens becomes an (infinitely thin) wetting film.

For elastic membranes with vanishing E_B, but finite Y_{2D}, the presence of additional elastic stresses makes the Laplace–Young equation inapplicable. However, it is intuitively clear that adding a thin elastic membrane onto a droplet should not affect its shape drastically, such that the elastic lens should consist of approximate spherical caps as well. This is corroborated by our numerically calculated shapes in Fig. 4 (left), which appear to be similar to liquid lens shapes composed of two spherical caps. We will exploit this similarity for an analytical approximation.

A closer inspection (see Appendix C.2) reveals that strictly spherical caps with a hemispherical rest shape do not allow for local force balance over the complete surface. However, we find an approximation analogous to the droplet by assuming uniform

(but anisotropic) strains along the contour. Geometrically, these strains are found to be

$$\lambda_s = \frac{2\theta(\tilde{h})}{\pi}\tilde{R}(\tilde{h}) \quad \text{and } \lambda_\phi = \tilde{R}_B = \tilde{R}(\tilde{h})\sin(\theta(\tilde{h})). \tag{13}$$

Inserting these approximative strains in the constitutive relations (4) we obtain the stress τ_s as a function of $\tilde{h}$. Using the Neumann condition (41) for force balance in the r-direction, we then find (see Appendix C.2)

$$\sigma = 2\tau_s(\tilde{h})\cos\theta(\tilde{h}) = 4\tau_s(\tilde{h})\frac{1-\tilde{h}^3}{2+\tilde{h}^3}, \tag{14}$$

where $\cos\theta(\tilde{h})$ is given by the geometric relation (11). Similarly to (12), solving this equation for $\tilde{h}$ gives the reduced height $\tilde{h}$ and, thus, also the contact angle θ as a function of σ/γ and γ/Y_{2D}.

We compare our analytical results for height $\tilde{h}$ and opening angle θ to numerical solutions of the shape eqn (5) in Fig. 5(A and B). The result (12) for the height of liquid lenses is in good agreement with solutions for elastic membrane lenses in the corresponding limit $\gamma \gg Y_{2D}$. Solutions of (14) for the height are in good agreement with numerical simulations within the range of the fluid and the crossover regime, *i.e.*, for $\gamma \geq Y_{2D}$. Even for $\gamma \leq Y_{2D}$ we find acceptable agreement. Note that only the dimensionless height $\tilde{h}$ can directly be determined for elastic shells, since the shape is rounded at the AB-interface. The solutions we obtain from (14) violate, however, the force balance condition, which explicitly demonstrates that already a simple Hookean stretching energy leads to non-trivial shapes.

3.2 Elastic shells: interface curvature

Microcapsules with elastic shells, *i.e.*, in the presence of an additional bending rigidity, exhibit lens-like shapes with rounded kinks at the AB-interface.

For decreasing bending moduli the rounded kink at the AB-interface becomes increasingly sharp and approaches the elastic lens shape suggesting a systematic relation between the interface curvature and the bending modulus which might allow for inferring the bending modulus from the shape profile. We quantify this in Fig. 5(C) showing the curvature κ_s at the liquid–liquid interface as a function of ${E_B}^{-1/2}\sigma^{3/2}$, where we clearly find a linear relationship implying $\kappa_s \propto {E_B}^{-1/2}\sigma^{3/2}$ in the elastic regime $\gamma/Y_{2D} \approx 0$. This scaling can be rationalized by an argument, which is similar to the Pogorelov theory for the rounding of the rim of a buckled elastic spherical shell by bending rigidity.[52,53] Details of this argument can be found in Appendix C.3. The essential idea is to consider the rounding of the sharp cusp present for an elastic lens with contact or opening angle θ and a complementary angle $\alpha = \pi/2 - \theta$, after introduction of a finite bending rigidity. Thus, we only have to consider the deviation from the rather simple elastic lens shape on a typical length scale ξ that is found from balancing stretching and bending contributions, from which we find the indicated scaling of the curvature $\kappa_s = \alpha/\xi$. The change in the bending energy scales as $U_B = E_B R_D \alpha^2/\xi^2$ whereas the interfacial contribution scales as $U_\sigma = \pi R_D \sigma \xi \alpha$, where R_D is the radius of the interface cross-section. Balancing both energies leads to $\xi \sim \alpha^{1/2}{E_B}^{1/2}\sigma^{-1/2}$ or $\kappa_s \sim \alpha^{1/2}{E_B}^{-1/2}\sigma^{1/2}$, which already proves $\kappa_s \propto {E_B}^{-1/2}$, but still depends on the angle α. The scaling of α is obtained from the Neumann condition (14), $\sigma = 2\tau_s(\tilde{h})\sin\alpha$, and depends on whether the surface tensions (fluid regime, $\alpha \sim \sigma/\gamma$) or the Young's modulus (elastic regime, $\alpha \sim (\sigma/Y_{2D})^{1/3}$) constitutes the dominant stretching force. This results in the final result for the curvature scaling,

$$\kappa_s \sim \begin{cases} {E_B}^{-1/2}\sigma^{2/3}\,{Y_{2D}}^{-1/6}, & \gamma \ll Y_{2D} \quad \text{(elastic)} \\ {E_B}^{-1/2}\sigma\gamma^{-1/2}, & \gamma \gg Y_{2D} \quad \text{(fluid)}, \end{cases} \tag{15}$$

which is in full agreement with the numerical results in Fig. 5(C). Note that the dependence on the bending modulus,

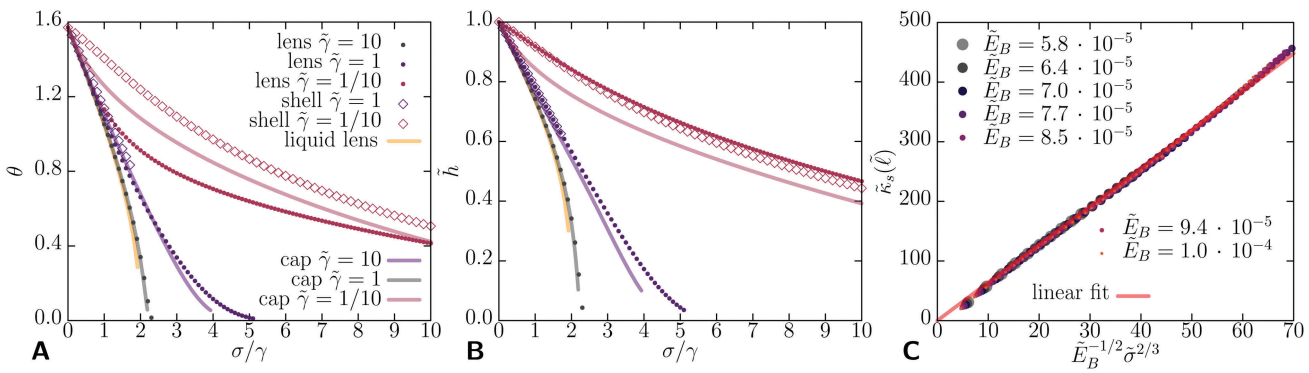

Fig. 5 (A) Contact angle $\theta = \psi^-(\ell) = \pi - \psi^+(\ell)$ as a function of the dimensionless tension $\tilde{\sigma}/\tilde{\gamma} = \sigma/\gamma$ for the symmetric case ($\gamma_A = \gamma_B$): comparison of liquid lens result (11) (yellow line) and spherical cap approximation (14) (red, purple, and gray lines) for the elastic lens with numerical results from solving the shape equations (red, purple, and gray dots). Spherical cap approximation and numerical results for the elastic lens are shown for three different regimes: (i) fluid regime $\tilde{\gamma} = \gamma/Y_{2D} \gg 1$ (gray), (ii) crossover regime $\tilde{\gamma} \sim 1$ (purple), and (iii) elastic regime $\tilde{\gamma} \ll 1$ (red). In addition, we compare with numerical results for shells with $\tilde{E}_B = 10^{-3}$ (open quads) for the crossover regime (purple), and the elastic regime $\tilde{\gamma} \ll 1$ (red). For shells, we use an effective opening angle θ_{eff}, which is obtained from the reduced height by the geometric relation $\cos\theta_{eff} = 2(1-\tilde{h}^3)/(2+\tilde{h}^3)$, for spherical caps. (B) Analogous comparison for the reduced height $\tilde{h} = h/R_0$ (using the same symbols). Numerical results for shells (open quads) in (A) and (B) show that even for shells of finite (though small) thickness the spherical cap approximation (14) works well. (C) Numerical verification of the scaling law $\tilde{\kappa}_s \sim \tilde{E}_B^{-1/2}\tilde{\sigma}^{2/3}$ for elastic shells in the purely elastic regime $\tilde{\gamma} = 0$, see eqn (15). All quantities are given in dimensionless form, $\tilde{\kappa}_s = \kappa_s R_0$, $\tilde{\sigma} = \sigma/Y_{2D}$, and $\tilde{E}_B = E_B/Y_{2D}{R_0}^2$.

$\kappa_s \propto E_B^{-1/2}$ is universal, *i.e.*, independent of whether we are in the fluid or the elastic regime. Switching from $E_B = 0$ to a finite E_B leads to a finite α and, thus, rounded edges.

Fig. 5(A) and (B) show that the analytical result (14) for the capsule height h and the effective opening angle, which is obtained *via* the geometrical relation $\cos\theta_{eff} = 2(1 - \tilde{h}^3)/(2 + \tilde{h}^3)$ for spherical caps, remain a good approximation also for microcapsules with elastic shells for small dimensionless bending rigidities ($\tilde{E}_B \sim 10^{-3}$ in Fig. 5(A) and (B)). This is also evident from Fig. 4, where shell and lens heights differ only slightly. Therefore, the parameters σ/γ and γ/Y_{2D} can be inferred from measurements of capsule heights over a wide range of elastic parameters by fitting with eqn (14) for the measured capsule heights.

Our result (15) for the curvature radius $1/\kappa_s$ at the rounded tip of an elastic shell then also suggests that the classical Neumann condition for symmetric liquid droplets, $\sigma = 2\gamma\cos\theta$, still holds for elastic shells and lenses as long as the curvature radius $1/\kappa_s$ at the rounded tip is small compared to the radius R_0 of the capsule, *i.e.*, for $1/\kappa_s R_0 \sim \tilde{E}_B^{1/2}\tilde{\sigma}^{-2/3} \ll 1$ (in the elastic regime $\tilde{\gamma} < 1$), if the approximative uniform stress $\tau_s(\tilde{h})$ is used as capsule-liquid surface tension γ, and if the effective Neumann angle θ_{eff} is used for θ. Similar observations have been made for the shapes of adhered vesicles,[54] which are also governed by the Young equation for liquid droplets with an effective surface tension as long as the contact curvature radius is small compared to the vesicle size. In Fig. 5(B), where $\tilde{E}_B = 10^{-3}$ (quads) and where we focus on the elastic regime $\tilde{\gamma} = 1/10$ and $\tilde{\gamma} = 1$, the condition $1/\kappa_s R_0 \sim \tilde{E}_B^{1/2}\tilde{\sigma}^{-2/3} \ll 1$ of small curvature radii is already fulfilled for $\tilde{\sigma}/\tilde{\gamma} \gg 10^{-5/4}$ and $\tilde{\sigma}/\tilde{\gamma} \gg 10^{-9/4}$, respectively.

3.3 Adsorption energy enhancement

Soft particles at liquid–liquid interfaces are efficient emulsifiers because they stretch during adsorption.[29] During deformation at the liquid–liquid interface a soft particle assumes a lens-like shape,[27,28] which increases the occupied interface area and, thus, decreases the interfacial energy, while the elastic energy increases. Typically, the elastic energy cost is smaller than the energy gain due to spreading within the interface, meaning that spreading is energetically preferable. The higher the interfacial energy gain $-\sigma\pi r^2(\ell)$ compared to the elastic cost (integrated energy density $w(s_0) - \gamma$), the more stable the interface becomes. The sum of the above two contributions is what we refer to as the adsorption energy. In ref. 55 the adsorption stability of nanoparticles at liquid–liquid interfaces has been investigated as a function of the particle shape, where it turns out that oblate shapes are most stable due to the high area occupation within the interface. Therefore, hollow elastic capsules with a thin elastic shell, which are much softer than filled particles, are very attractive candidates to further improve emulsification.

Using our numerical results we can quantify the increase in adsorption energy as a function of the softness of the capsule. The adsorption energy of a deformable capsule is given by the total energy gain if the capsule is moved from one of the liquid phases to the liquid–liquid interface,

$$\Delta E_{soft} = -\sigma\pi r^2(\ell) + \int (w(s_0) - \gamma)\mathrm{d}A_0, \qquad (16)$$

where $\pi r^2(\ell)$ is the occupied circular cross-section area within the liquid–liquid interface plane and the last term is the elastic energy including stretching energy, bending energy, and the change in surface energy $\gamma(A - A_0)$. Each capsule moving to the liquid–liquid interface lowers the interfacial energy by ΔE_{soft} and, thus, decreases the effective surface tension of the liquid–liquid interface.

This effect is stronger for hollow soft elastic capsules as compared to hard particles and becomes more pronounced with decreasing thickness of the capsule. For hard spherical particles of equal size we have an adsorption energy $\Delta E_{hard} = -\sigma\pi R_0^2$. In Fig. 6 we numerically quantify the adsorption energy difference between soft and hard particles,

$$\Delta(\Delta E) \equiv \Delta E_{soft} - \Delta E_{hard}, \qquad (17)$$

as a function of the dimensionless bending modulus $\tilde{E}_B = H^2/12(1 - \nu_{2D}^2)R_0^2$, which characterizes the thickness of the capsule, see eqn (2). This allows us to quantify the relative enhancement of the adsorption energy due to capsule softness by decreasing $\tilde{E}_B$ or the capsule thickness. For $\tilde{E}_B \sim 10$ (corresponding to $H \sim R_0$ and $\nu_{2D} = 1/2$) the results should become similar to the energy gain for soft filled particles as they have been considered in ref. 27–29. Fig. 6 then clearly shows that hollow capsules are much more efficient as emulsifiers than filled soft particles (or even a filled hard particle) of equal size.

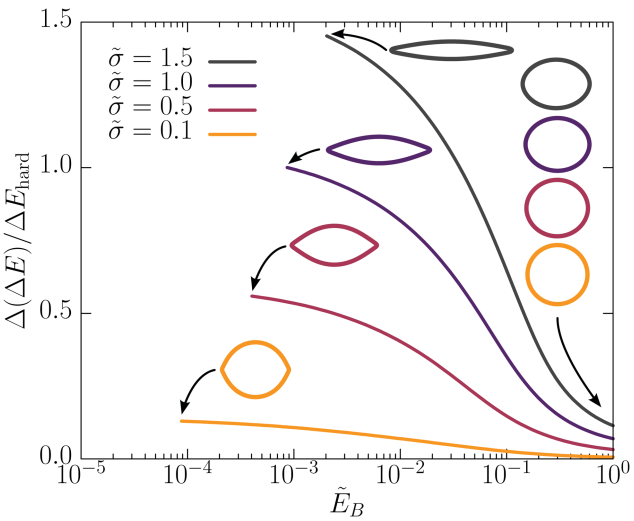

Fig. 6 Normalized adsorption energy difference $\Delta(\Delta E)/\Delta E_{hard}$ between soft and hard particles as a function of the dimensionless bending rigidity $\tilde{E}_B \sim H^2/R_0^2$ for different values of the dimensionless liquid tension $\tilde{\sigma} = \sigma/Y_{2D}$. $\Delta(\Delta E)/\Delta E_{hard} = 1$ is equivalent to a 100% enhancement of the adsorption energy difference of a soft capsule compared to a hard particle. The adsorption energy is strongly enhanced for hollow capsules with small thickness to radius ratios H/R_0 and for large liquid tensions. For the above measurement we used $\gamma/Y_{2D} = 1/10$. The insets show exemplary shapes for different values of $\tilde{E}_B$ and $\tilde{\sigma}$.

4 Discussion and conclusion

We investigated shapes of deformed microcapsules adsorbed at liquid–liquid interfaces. We mainly focused on the situation where capsules are stretched by a liquid–liquid interface outside the capsule, see Fig. 1(A), but our numerical methods (including matching conditions) are equally applicable to compressive tension, which arise, if a liquid–liquid interface is formed inside the capsule, see Fig. 1(B). We demonstrated this in Fig. 4, where we present numerical results for both cases.

Gravitational effects can be generically neglected for micrometer-sized capsules because both the capillary length $L_c = (\sigma/\Delta\rho g)^{1/2}$ and the gravitational elastocapillary length $L_g = (Y_{2D}/\Delta\rho g)^{1/2}$ are in the millimeter range exceeding capsule size. We showed in Section 2.7, how our model can be extended to include all gravitational effects if larger, millimeter-sized capsules are considered in future work.

The deformability of hollow microcapsules by the liquid–liquid interfacial tension mainly depends on their thickness H. For hollow capsules with a soft shell strains become large if $\sigma > Y_{2D} \sim Y_{3D}H$, *i.e.*, if the shell thickness H is sufficiently small compared to the elastocapillary length $L_\sigma = \sigma/Y_{3D}$. For a typical soft capsule shell material with $Y_{2D} \sim 10^{-2}\ldots10^{-1}$ N m^{-1}, liquid–liquid interfacial tensions $\sigma > 10^{-2}$ N m^{-1} are sufficient to induce considerable (but not large) strains, which can be realized by oil–water interfaces.

Shapes of deformed capsules with spherical rest shapes are lens-like if they are stretched at a liquid–liquid interface; in the presence of bending rigidity the edge of the lenticular shape is rounded. Neglecting gravitation we derived shape equations and matching conditions at the liquid–liquid interface for the numerical calculation of these shapes for extensible shells of finite thickness and constant volume, as well as for two important limiting cases, namely elastic lenses (zero bending modulus) and liquid lenses (zero Young's and bending moduli, only surface tension). We calculated numerical solutions for each of these cases, see Fig. 4. We also derived analytical approximations for characteristics of the deformed capsule shapes in agreement with our numerical results.

Our approximative theory based on spherical cap shapes can be used to determine Young's modulus Y_{2D} and the pressure p_0 from a single measurement of the cap height h or the contact angle θ, if the surface tensions σ and γ are known, see Fig. 5(A and B). Two height measurements of the same capsule at different surface tensions σ or at different capsule volumes V_0 could be used to determine both Young's modulus Y_{2D} and the capsule-liquid surface tension γ (assuming values for the Poisson ratio, for example, $\nu_{2D} = 1/2$).

This could be further extended, and our scheme for numerical calculation of shapes can, in principle, be used for elastometry, *i.e.*, to determine elastic moduli from an experimentally acquired image by fitting numerical solutions of the shape equations to a set of contour points extracted from the image. Other elastometry methods following the same philosophy are the study of deformations of pendant capsules under volume changes to obtain elastic moduli as investigated in ref. 32–34, the study of the edge curvature of buckled shapes to obtain the bending modulus,[35] or the study of shapes of osmotically buckled capsules to infer the osmotic pressure.[36]

For shells of finite thickness we also found an analytical result for the maximal curvature at the ''tips'' of the rounded lens in terms of the bending modulus, Young's modulus and the interface load, see eqn (15) and Fig. 5(B). Also this analytical result can be used in several ways to extract information on elastic moduli from a measurement of the shell's curvature κ_s at the interface and if the interface load σ from the liquid–liquid surface tension is known. If Young's modulus Y_{2D} of the capsule material is known (for example, from other elastometry methods[32–34]) we can determine the bending modulus by

$$E_B = 40.9 {Y_{2D}}^{-1/3} \sigma^{4/3} {\kappa_s}^{-2}. \tag{18}$$

If the shell thickness H is known we can determine the bending modulus or Young's modulus by

$$\begin{aligned} E_B &= 9.3 H^{1/2} \sigma {\kappa_s}^{-3/2}, \\ Y_{2D} &= 84.1 H^{-3/2} \sigma {\kappa_s}^{-3/2}, \end{aligned} \tag{19}$$

where we used $\nu_{2D} = 1/2$. The numerical prefactors in eqn (18) and (19) were determined by a linear fit to the numerical results and we used relation (1) for E_B and Y_{2D}. Note that $\sigma {\kappa_s}^{-3/2} =$ const., which is why it makes sense to vary the interface load σ in order to improve the statistical significance of such a measurement. This could be achieved by, *e.g.*, adding surfactants to one of the liquid phases A or B that decrease σ with increasing surfactant concentration. The dependence of σ and the surfactant concentration can be determined, *e.g.*, in a pendant drop tensiometer. The curvature κ_s can be obtained from analyzing capsule images and fitting a circle to the capsule edge at the liquid–liquid interface. Using typical values for soft microcapsules ($E_B = 10^{-16}\ldots10^{-14}$ N m, $Y_{2D} = 10^{-2}\ldots10$ N m^{-1} corresponding to $H = 0.03\ldots3$ μm) and a liquid–liquid interfacial tension (*e.g.* oil–water) of $\sigma \sim 5 \times 10^{-2}$ N m^{-1}, we expect curvature radii $1/\kappa_s \sim 0.005\ldots0.1$ μm according to (18), which can be measured optically as has been demonstrated in ref. 56.

In conclusion, the results presented in this paper allow us, in principle, to determine the full set of elastic constants from shape profiles of elastic capsules adsorbed to liquid–liquid interfaces. To realize this setup experimentally, several problems have to be solved. One main problem will be to find a liquid–liquid interface with sufficiently high surface tension such that the condition $\sigma > |\gamma_A - \gamma_B|$ for adsorption of the capsule to the interface is fulfilled and such that the observed strains $\Delta R/R_0 \sim \sigma/Y_{2D}$ and, thus, the capsule deformation are observable. Another problem might be leakage through the capsule membrane, while we assume a fixed volume in the present calculation. A known shrinking volume can, however, be included in the present approach by introducing a corresponding decreasing internal pressure p_0.

Finally, we could show that hollow elastic microcapsules can be much more effective in reducing the interfacial energy than filled soft particles or even hard particles of the same size,

see Fig. 6. During capsule deformation at the liquid–liquid interface into a lens-like shape the adsorption energy, which results from the balance of the occupied liquid–liquid interface area and the elastic energy of the capsule shell, increases significantly. In Fig. 6 we compare hollow capsules, filled soft particles and hard particles of equal size R_0. The effectiveness of hollow capsules in reducing the interfacial energy can also be appreciated by comparing with particles of equal deformability: a hollow capsule with shell thickness H exhibits a similar elastic deformation to a filled soft particle of size H. The size of the hollow microcapsule can be made much larger, however, in order to achieve a much larger occupied liquid–liquid interface area as compared to the filled particle. This leads to much higher adsorption energies at comparable softness. We conclude that hollow microcapsules could be much more efficient in foam and emulsion stabilization than filled particles of comparable size or comparable softness.

Conflicts of interest

There are no conflicts to declare.

Appendix

A Shape equation approach

In this section, we give details of the derivation of the shape eqn (5) by variational energy minimization. We give a detailed derivation of the matching conditions at the liquid–liquid interface and present details on the numerical solution of the shape equations.

A.1 Shape equations

A.1.1 Variational approach. We calculate the first variation and the resulting Euler–Lagrange equations for the free energy functional (6) by variation with respect to the functions $r(s_0)$ and $\psi(s_0)$. First we perform the variation of

$$\begin{aligned} G_0 &= \int w(s_0)\mathrm{d}A_0 - p_0 V = \int_0^{L_0} \mathrm{d}s_0 g \quad \text{with} \\ g &\equiv 2\pi r_0 w - p_0 \pi r^2 \lambda_\mathrm{s} \sin\psi \end{aligned} \tag{20}$$

in the absence of the interface load $E_\sigma = -\sigma\pi r^2(\ell)$ (we repeat this calculation from Appendix A in ref. 35 for completeness of the presentation), in order to derive the shape equations for the upper and lower parts of the capsule. In Appendix A.2 we include E_σ to derive the matching conditions at the three phase contact line joining the upper and lower parts of the capsule. Assuming an incompressible liquid within the capsule and an impermeable membrane leads to conservation of the capsule volume

$$V = \int \pi r^2 \mathrm{d}z = \int_0^{L_0} \pi r^2 \lambda_\mathrm{s} \sin\psi \mathrm{d}s_0 = V_0 = \frac{4\pi}{3} {R_0}^3, \tag{21}$$

where R_0 is the radius of the spherical equilibrium shape of the capsule. The volume constraint $V = V_0 = \text{const}$ is included by adjusting the hydrostatic pressure p_0 as a Lagrange parameter.

Using the definition of the stresses and bending moments (see first equalities in eqn (4); in the following, $f' \equiv \mathrm{d}f/\mathrm{d}s_0$) for the variation of the elastic energy density,

$$\begin{aligned} \delta w &= \lambda_\phi \tau_\mathrm{s} \delta e_\mathrm{s} + \lambda_\mathrm{s} \tau_\phi \delta e_\phi + \lambda_\phi m_\mathrm{s} \delta K_\mathrm{s} + \lambda_\mathrm{s} m_\phi \delta K_\phi \quad \text{with} \\ \delta e_\mathrm{s} &= \frac{\delta r'}{\cos\psi} + \lambda_\mathrm{s} \tan\psi \delta\psi, \quad \delta e_\phi = \frac{1}{r_0}\delta r, \\ \delta K_\mathrm{s} &= \delta\psi', \quad \delta K_\phi = \frac{\cos\psi}{r_0}\delta\psi, \end{aligned} \tag{22}$$

and

$$\delta(r^2 \lambda_\mathrm{s} \sin\psi) = 2r\lambda_\mathrm{s} \sin\psi \delta r + r^2 \tan\psi \delta r' + \frac{\lambda_\mathrm{s} r^2}{\cos\psi}\delta\psi \tag{23}$$

for the variation of the volume, we find the first variation of the free energy G

$$\begin{aligned} \delta G_0 &= \int_0^{L_0} \mathrm{d}s_0 2\pi \Big(\delta r \{ \lambda_\mathrm{s}\tau_\phi - p_0 r \lambda_\mathrm{s} \sin\psi \} \\ &\quad + \delta r' \left\{ \frac{r\tau_\mathrm{s}}{\cos\psi} - \frac{p_0}{2} r^2 \tan\psi \right\} \\ &\quad + \delta\psi \left\{ r\tau_\mathrm{s}\lambda_\mathrm{s} \tan\phi - \frac{p_0}{2}\frac{\lambda_\mathrm{s} r^2}{\cos\psi} + \lambda_\mathrm{s} m_\phi \cos\psi \right\} + \delta\psi' \{ r m_\mathrm{s} \} \Big) \end{aligned}$$

or

$$\delta G_0 = \int_0^{L_0} \mathrm{d}s_0 \Big(\delta r g_\mathrm{r} + \delta r' g_{r'} + \delta\psi g_\psi + \delta\psi' g_{\psi'} \Big) \quad \text{with} \tag{24}$$

$$\begin{aligned} g_r &\equiv 2\pi\lambda_\mathrm{s}(\tau_\phi - p_0 r \sin\psi), \quad g_{r'} \equiv 2\pi(-rq \sin\psi + r\tau_\mathrm{s}\cos\psi) \\ g_\psi &\equiv 2\pi\lambda_\mathrm{s}(-rq + m_\phi \cos\psi), \quad g_{\psi'} \equiv 2\pi r m_\mathrm{s}, \end{aligned} \tag{25}$$

where we also defined

$$q \equiv -\tau_\mathrm{s} \tan\psi + \frac{1}{2} p_0 \frac{r}{\cos\psi}. \tag{26}$$

Partial integration in eqn (24) gives two standard Euler–Lagrange equations

$$\text{(i) } g_r = \frac{\mathrm{d}}{\mathrm{d}s_0} g_{r'}, \quad \text{(ii) } g_\psi = \frac{\mathrm{d}}{\mathrm{d}s_0} g_{\psi'} \tag{27}$$

on the interval $s_0 \in [0, L_0]$. Using $\lambda_\mathrm{s} = \mathrm{d}s/\mathrm{d}s_0$ and the geometric relations $\mathrm{d}r/\mathrm{d}s = \cos\psi$ and $\mathrm{d}\psi/\mathrm{d}s = \kappa_\mathrm{s}$, which follow from the definition of the slope angle ψ (see Fig. 7(B)), these Euler–Lagrange equations can be re-arranged to give

$$\begin{aligned} \text{(i) } 0 &= -\frac{\cos\psi}{r}\tau_\phi + \frac{1}{r}\frac{\mathrm{d}(r\tau_\mathrm{s})}{\mathrm{d}s} - \kappa_\mathrm{s} q, \\ \text{(ii) } 0 &= \frac{\cos\psi}{r} m_\phi - \frac{1}{r}\frac{\mathrm{d}(r m_\mathrm{s})}{\mathrm{d}s} - q, \end{aligned} \tag{28}$$

which represents (i) stress equilibrium in the tangential direction and (ii) torque (bending moment) balance[35,43] that has to hold for any interface patch, see Fig. 7(A). Moreover, the definition (26) of the normal transverse shear force density q

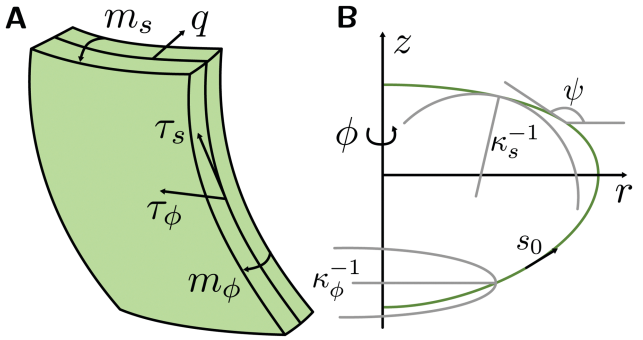

Fig. 7 (A) Forces and torques acting on an infinitesimal membrane patch. Both forces and torques are integrated over the thickness H of the material, which is assumed to be constant. (B) Shape profile given by the shape equations. The shape profile generates a surface of revolution describing a three-dimensional axisymmetric object. The curvatures κ_ϕ and κ_s determine the local bending energy.

can be used to derive (together with (i)) the normal stress equilibrium[35,43]

$$\text{(iii)}\ 0 = -p_0 + \kappa_\phi \tau_\phi + \kappa_s \tau_s + \frac{1}{r}\frac{\mathrm{d}(rq)}{\mathrm{d}s}, \qquad (29)$$

In order to obtain a closed set of shape equations, we also use the geometric relations

$$r'(s_0) = \lambda_s \cos\psi, \quad z'(s_0) = \lambda_s \sin\psi, \quad \psi'(s_0) = \lambda_s \kappa_s, \qquad (30)$$

(see Fig. 7(B)). Using $\lambda_s = \mathrm{d}s/\mathrm{d}s_0$ to relate deformed to undeformed arc length, eqn (28)–(30) are equivalent to the shape eqn (5) in the main text. To convert these shape equation system into actual geometric shapes constitutive relations are needed, which we address in the following part. Additional external shear and normal pressures (see Appendix A.1.3 below) p_s and p_n, respectively, can be included as additional contributions, $-p_s$ on the right hand side of the tangential stress equilibrium (i) and $-p_n$ on the right hand side of the normal stress equilibrium (iii). Instead we will include E_σ in the free energy and derive matching conditions from variational calculus in Appendix A.2.

A.1.2 Hookean elasticity and alternative constitutive relations. The shape equations in the form (5) are still independent of the elastic material law. They only contain stress and moment equilibria and geometrical relations and no information on the constitutive relation characterizing the material. The constitutive relations are needed to close the shape equations as described in the main text. We use nonlinear Hookean elasticity with constitutive eqn (4), which derive from the Hookean elastic energy (3).

For large stretching tensions σ such that $\sigma > Y_{2D}$ ($H < L_\sigma$) and $\sigma > \gamma$, the stretching strains $e_{s,\phi} = (\lambda_{s,\phi}{}^2 - 1)/2$ are no longer small and the linear approximation $e_{s,\phi} \approx \lambda_{s,\phi} - 1$ breaks down. Then the essentially linear Hookean constitutive relation (4) is no longer valid and has to be replaced by more specific nonlinear hyperelastic material laws, such as Mooney–Rivlin or Skalak laws.[43,48] For the Mooney–Rivlin law it has been explicitly demonstrated in ref. 34 as to how this constitutive relation can be used to close the shape eqn (5). Because the shape eqn (5) are closed by eliminating λ_s and τ_ϕ by using the constitutive relations for stresses and strains, nonlinear relations such as Mooney–Rivlin laws are considerably more difficult to handle and lead to larger computational cost.[34]

In Fig. 8, we investigate in more detail whether nonlinear effects can play a role in capsules stretched with tensile stresses $\sigma \leq Y_{2D}$, which are realistic for typical experimental situations and also used for the shape evolutions in Fig. 4. We find that meridional strains remain small, whereas circumferential stresses can indeed become large locally in the vicinity of the liquid–liquid interface (reaching values $\lambda_\phi \simeq 1.8$ for $\sigma = Y_{2D}$). This will lead to a further stretching of the capsule shape if, for example, a more realistic Mooney–Rivlin elastic law is used which displays a softening for large strains.[48] We do not expect, however, that any of our results will qualitatively change if more realistic nonlinear elastic laws are used in this regime.

Another problem arises if compressive stresses $\tau_s < 0$ or $\tau_\phi < 0$ occur, which can give rise to wrinkle formation, and require a different effective constitutive relation in the compressed region.[32,34] We have checked explicity that such compressive stresses do not occur for capsules stretched at a liquid–liquid interface, *i.e.*, $\sigma > 0$. For compressive tensions $\sigma < 0$, compressive stresses $\tau_\phi < 0$ can indeed occur, such that wrinkles in the s-direction could form in the vicinity of the AB-interface. We do not include wrinkle formation in our analysis as we focus on tensile stresses $\sigma > 0$ throughout this paper.

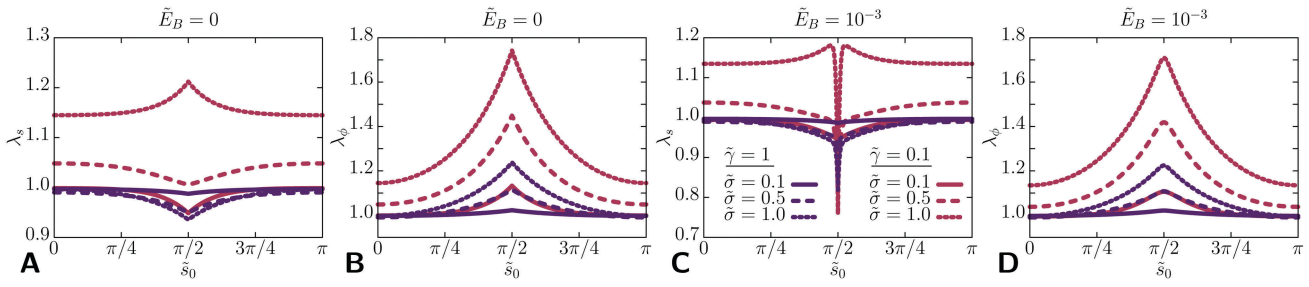

Fig. 8 Stretching ratios λ_s (A and C) and λ_ϕ (B and D) along the capsule contours for $\tilde{E}_B = 0$ (A and B) and $\tilde{E}_B = 10^{-3}$ (C and D) in the elastic regime $\gamma/Y_{2D} = \tilde{\gamma} = 1/10$ (red) and the crossover regime $\tilde{\gamma} = 1$ (purple) and for different tensile stresses $\tilde{\sigma} = \sigma/Y_{2D}$ for the symmetric case. Whereas meridional strains $|\lambda_s - 1| < 0.2$ remain small in (A and C), circumferential strains $|\lambda_\phi - 1|$ can become large at the liquid–liquid interface, where tension is exerted. In the elastic regime $\tilde{\gamma} = 1/10$, values $\lambda_\phi \simeq 1.8$ are reached for $\tilde{\sigma} = 1$.

A.1.3 Pressure and external forces. Assuming an incompressible liquid within the capsule and an impermeable membrane leads to conservation of the capsule volume (21). The volume constraint $V = V_0 = \text{const}$ is satisfied by adjusting the hydrostatic pressure p_0, which serves as a Lagrange parameter. In practice, the volume constraint is realized by including it in the shooting method, *i.e.*, by using p_0 as the shooting parameter to obtain a given volume V_0 at the end of the integration along the contour.

If p_0 is not interpreted as a Lagrange parameter we have actual pressure control. Then the pressure p_0 is prescribed and determines the capsule volume $V = V(p_0)$. Solutions for pressurized capsules are numerically simpler to obtain and possibly exhibit more diverse shapes due to the lacking volume constraint. Another possibility, which is intermediate between pure pressure and pure volume control, is osmotic pressure control.[36] Then the osmotic pressure inside the capsule becomes a function of the capsule volume $p_0 = p_0(V)$, the shape of which depends on the osmolyte concentration. We restrict ourselves here to capsules with a constant volume in which the hydrostatic pressure adapts accordingly.

External forces arise from the surface tension of the AB-interface which act along the contact line $z = 0$ at arc length $s_0 = \ell$ around the capsule. This can be interpreted as a point load on the capsule contour, *i.e.*, a localized force density (7).

The force density could be included as a pressure contribution into the shape eqn (5) leading to normal and tangential pressure contributions

$$p_\mathrm{n} = \vec{f}_\sigma \cdot \vec{n} = \sigma\delta(s_0 - \ell)\sin\psi,$$
$$p_\mathrm{s} = -\vec{f}_\sigma \cdot \vec{e}_\mathrm{s} = -\sigma\delta(s_0 - \ell)\cos\psi, \qquad (31)$$

The total normal pressure is then given by $p = p_0 + p_\mathrm{n}$. We will rather include the point loads by deriving adequate matching conditions for the forces τ_s and q at $z = 0$ or $s_0 = \ell$ from variation of the energy (6) in the following Section A.2.

A.2 Matching conditions at the liquid–liquid interface. At the liquid–liquid interface at $z = 0$ and $s_0 = \ell$ the shape eqn (5) have to be complemented by matching conditions. We argued in the main text that six matching conditions are needed for a Hookean shell, whose shape is obtained by the full set (5) of six shape equations, whereas only four matching conditions are needed for a Hookean membrane, which is described by four shape equations ($m_\mathrm{s} = 0$ and $q = 0$ in eqn (5)). Moreover, we need to determine the parameter ℓ itself by energy minimization in the general asymmetric case. For the symmetric case $\gamma_\mathrm{A} = \gamma_\mathrm{B}$ we have $\ell = L_0/2$ by symmetry. The capsule consists of two solution branches $z > 0$ and $z < 0$, for which we will use superscripts + and −, respectively, in the following to formulate the matching conditions.

We will derive all matching conditions from continuity conditions for intact closed shells and variation of the energy (6) with respect to the position of the three phase contact line at $z = 0$ and $s_0 = \ell$.

We have three obvious matching conditions for z and r,

$$z^+(\ell) = z^-(\ell) = 0 \quad \text{and } r^+(\ell) = r^-(\ell) \equiv r(\ell), \qquad (32)$$

from requiring a closed capsule. The two matching conditions for z fix the shooting parameters $z(0)$ and $z(L_0)$. From continuity of r also the continuity of $\lambda_\phi = r/r_0$ follows immediately. For a shell with bending rigidity we also have the fourth matching condition

$$\psi^+(\ell) = \psi^-(\ell) \qquad (33)$$

because a kink in the capsule shell costs an infinite bending energy. Membranes and droplets, however, will exhibit such kinks and $\psi^+(\ell)$ and $\psi^-(\ell)$ can freely adjust. From continuity of r and ψ, also the continuity of the curvature $\kappa_\phi = \sin\psi/r$ follows.

All remaining matching conditions are derived based on the variational calculus introduced in ref. 35 by minimizing the total free energy $G = \int w(s_0)\mathrm{d}A_0 - p_0 V - \sigma\pi r^2(\ell)$ or (using eqn (21))

$$G = \int_0^\ell \mathrm{d}s_0 g^- + \int_\ell^{L_0} \mathrm{d}s_0 g^+ - \sigma\pi r(\ell)^2, \quad \text{with}$$
$$g^\pm \equiv 2\pi r_0 w^\pm - p_0\pi(r^\pm)^2\lambda_\mathrm{s}^\pm \sin\psi^\pm, \qquad (34)$$

where $w^\pm(s_0)$ are the Hookean energy densities (3) of the upper and lower parts of the capsule, which have identical elastic constants Y_2D, ν_2D, and E_B but differ in their surface tension contributions with γ_A in the lower (−) and γ_B in the upper (+) part; the energy $E_\sigma = -\sigma\pi r^2(\ell)$ is the potential for the point force $\vec{f}_\sigma$ from eqn (7). The free energy G has to be extremized with respect to the functions $r^\pm(s_0)$ and $\psi^\pm(s_0)$ as well as with respect to the location ℓ of the liquid–liquid interface. The total variations $\delta r \equiv (r + \delta r)(\ell + \delta\ell) - r(\ell) = \delta r(\ell) + r'(\ell)\delta\ell$ and $\delta\psi \equiv (\psi + \delta\psi)(\ell + \delta\ell) - \psi(\ell) = \delta\psi(\ell) + \psi'(\ell)\delta\ell$ at the variable interface position ℓ have to fulfill the continuity conditions $\delta r^- = \delta r^+$ and, for a shell, $\delta\psi^- = \delta\psi^+$.

Extremizing with respect to the functions $r^\pm(s_0)$ and $\psi^\pm(s_0)$ leads to the same Euler–Lagrange eqn (27) or (28), which hold both for the upper (+) and lower (−) parts. In variational calculus with variable functions at the boundary at $s_0 = \ell$, each continuity condition at the boundary entails a corresponding Weierstrass–Erdmann condition. Equating all boundary terms $\propto \delta r^+ = \delta r^-$ in the variation δG to zero we obtain the Weierstrass–Erdmann condition for r

$$0 = g^-_{r'}|_\ell - g^+_{r'}|_\ell + \frac{\mathrm{d}}{\mathrm{d}r(\ell)}E_\sigma = g^-_{r'}|_\ell - g^+_{r'}|_\ell - r(\ell)\sigma. \qquad (35)$$

Likewise, equating all boundary terms $\propto \delta\psi^+ = \delta\psi^-$ in the variation δG to zero for shells, we find the Weierstrass–Erdmann condition for ψ

$$0 = g^-_{\psi'}|_\ell - g^+_{\psi'}|_\ell + \frac{\mathrm{d}}{\mathrm{d}\psi(\ell)}E_\sigma = g^-_{\psi'}|_\ell - g^+_{\psi'}|_\ell. \qquad (36)$$

Moreover, because of the variable interface position we also have to equate all boundary terms $\propto \delta\ell$ in the variation δG to zero (at constant volume), which gives an additional

transversality condition

$$\left(g^{+}-(r^{+})'g^{+}_{r'}-(\psi^{+})'g^{+}_{\psi'}\right)|_{\ell}=\left(g^{-}-(r^{-})'g^{-}_{r'}-(\psi^{-})'g^{-}_{\psi'}\right)|_{\ell}, \tag{37}$$

where the ψ-terms are only present for shells.

As derived above in eqn (26), variation of G gives the additional algebraic relation

$$q\cos\psi+\tau_{\mathrm{s}}\sin\psi=\frac{1}{2}p_0 r, \tag{38}$$

for $s_0 \neq \ell$, which can replace the shape equation for q in (5). This algebraic equation is equivalent to force equilibrium in the z-direction for any part of the capsule from the lower apex up to arc length s. In equilibrium, the total force F_z in the axial z-direction that acts on the lower part of the capsule from the lower apex up to arc length s vanishes because of axial symmetry and the absence of external forces such as gravity acting in the z-direction,[41,42]

$$\begin{aligned}0 \;&= F_z(s)=2\pi r(q\cos\psi+\tau_{\mathrm{s}}\sin\psi)\\ &\quad-2\pi\int_0^s \mathrm{d}\tilde{s}r((p_0+p_{\mathrm{n}})\cos\psi+p_{\mathrm{s}}\sin\psi)\\ &=2\pi r(q\cos\psi+\tau_{\mathrm{s}}\sin\psi)-\pi p_0 r^2,\end{aligned} \tag{39}$$

where we used eqn (31) for p_{n} and p_{s} to obtain the last equality. The first term is the total interfacial force in the z-direction integrated along the rim of length $2\pi r$, and the second part is the total pressure force acting on the area of the lower capsule part in the z-direction. There are no additional forces in the z-direction from the liquid–liquid interface such that both contributions must cancel for all s, also at the liquid–liquid interface at $s = \ell$.

Eqn (38) also implies that $q = 0$ at the apices where $r = 0$ and $\psi = 0$ or π, which justifies the boundary conditions $q(0) = q(L_0) = 0$. At the interface at $s_0 = \ell$ the right hand side of eqn (38) is continuous because r is continuous, $r^{+}(\ell) = r^{-}(\ell) = r(\ell)$ such that

$$\left(q^{+}\cos\psi^{+}+\tau_{\mathrm{s}}^{+}\sin\psi^{+}\right)\big|_{\ell}=\left(q^{-}\cos\psi^{-}+\tau_{\mathrm{s}}^{-}\sin\psi^{-}\right)\big|_{\ell}=\frac{1}{2}p_0 r(\ell). \tag{40}$$

This is equivalent to $F_z^{+}(\ell) = F_z^{-}(\ell) = 0$, which holds because the liquid–liquid interface exerts no force in the z-direction. The first equality in eqn (40) describes a force equilibrium in the z-direction at the contact line between the capsule and liquid interfacial tensions and, thus, follows from a Neumann triangle construction (see also Fig. 2). The liquid–liquid interface does not exert interfacial forces in the z-direction and, thus, σ does not enter eqn (40); discontinuities in the normal shear force density q and in the tangential force density τ_{s} have to cancel in the z-direction.

The second equality in eqn (40) shows that the continuity of $r^{+}(\ell) = r^{-}(\ell) = r(\ell)$ is actually equivalent to the Neumann tension force equilibrium in the z-direction at the contact line because continuity of r leads to continuity of the pressure force $\pi p_0 r^2$ in the z-direction and interfacial and pressure forces are always opposite and equal according to the relation $F_z(s) = 0$ for the total force. Therefore, using both matching conditions (40) and $r^{+}(\ell) = r^{-}(\ell) = r(\ell)$ always leads to an over-determined set of matching conditions.

Using the definitions (25) in the Weierstrass–Erdmann condition (35) from the variation $\delta r^{-} = \delta r^{+}$ at the boundary gives

$$(q^{+}\sin\psi^{+}-\tau_{\mathrm{s}}^{+}\cos\psi^{+})|_{\ell}=(q^{-}\sin\psi^{-}-\tau_{\mathrm{s}}^{-}\cos\psi^{-})|_{\ell}+\sigma, \tag{41}$$

which describes the force equilibrium in the radial direction at the contact line between the capsule and liquid interfacial tensions and, thus, also follows from the Neumann triangle construction (see also Fig. 2). Discontinuities in the normal shear force density q and in the tangential force density τ_{s} in the r-direction have to cancel with the tension σ, which also acts in the r-direction.

Likewise, using the definitions (25) in the Weierstrass–Erdmann condition (36) from the variation $\delta\psi^{-} = \delta\psi^{+}$ at the boundary gives

$$m_{\mathrm{s}}^{+}(\ell)=m_{\mathrm{s}}^{-}(\ell), \tag{42}$$

which holds for shells and describes the moment equilibrium at the contact line. Continuity of m_{s} and κ_ϕ (see above) also entails continuity of κ_{s} and m_ϕ and, thus, of the entire bending energy density.

Inserting the definitions (25) in the transversality condition (37) and also utilizing the continuity of r (and m_{s} and κ_{s} for shells) and the first equation from the force equilibrium in the z-direction eqn (40) finally we find

$$(w^{+}-\lambda_{\mathrm{s}}^{+}\lambda_\phi^{+}\tau_{\mathrm{s}}^{+})|_{\ell}=(w^{-}-\lambda_{\mathrm{s}}^{-}\lambda_\phi^{-}\tau_{\mathrm{s}}^{-})|_{\ell}. \tag{43}$$

Because the bending energy part of w is continuous, it follows that the discontinuity in w across the interface is exactly due to the discontinuity in γ, which jumps from $\gamma^{-} = \gamma_{\mathrm{A}}$ for $z < 0$ to $\gamma^{+} = \gamma_{\mathrm{B}}$ for $z > 0$. This means, in turn, that the stretching elasticity part of w is also continuous. Because λ_ϕ is continuous (see above), λ_{s} is also continuous and, thus, the transversality condition (43) means that the elastic parts of the tensions $\tau_{\mathrm{s}} - \gamma$ and $\tau_\phi - \gamma$ have to be continuous across the interface,

$$(\tau_{\mathrm{s}}^{+}-\gamma^{+})|_{\ell}=(\tau_{\mathrm{s}}^{-}-\gamma^{-})|_{\ell}. \tag{44}$$

In our numerical treatment, we will not employ the transversality condition in the forms (43) or (44) but prefer to numerically minimize the total energy with respect to ℓ (changing the interface arc length ℓ for this minimization requires a re-meshing in the multiple shooting method that is explained in the next section).

A.3 Numerical method/precision. To achieve numerical stability we employ a multiple shooting method (Fig. 9), where we subdivide each solution branch into M segments. At each intermediate point we gain six shooting parameters and six continuity conditions (for the general shell case). The (−)-branch is integrated counter-clockwise over the interval $[0,\ell]$ starting at $s_0 = 0$ and ending at $s_0 = \ell$; the (+)-branch is integrated clockwise over $[\ell,L_0]$ starting at $s_0 = L_0$ and ending at $s_0 = \ell$. Both branches thus start at the axis of rotation and

match at the interface. When the interface arc length ℓ is changed, the segmentation of the shape has to be adapted, such that the (−)-branch is integrated over the intervals $[k\ell/M, (k+1)\ell/M]$ where $k = 0,\ldots,M-1$, and the (+)-branch is integrated over the intervals $[L_0-(k+1)(L_0-\ell)/M, L_0-k(L_0-\ell)/M]$. During the minimization (34) we iteratively change the segmentation of the shape, *i.e.*, change ℓ until the total free energy G reaches its minimum.

For the multiple shooting we employ a least squares minimization technique that minimizes the distances between the individual shape segments, the matching conditions at the interface, as well as the deviation from the target volume V_0. We therefore compute the Jacobian in order to obtain descent directions, that we follow iteratively. We assume that this algorithm is converged, if the Euclidean norm of the (dimensionless) residual vector falls below $\varepsilon = 10^{-8}$. This way we obtain valid solutions of the shape equations for a given branch junction length ℓ. Now, to obtain asymmetric shapes we need to minimize (34) by changing ℓ iteratively. Therefore, we use a one-dimensional method (similar method to that described above), which terminates on falling below a step length $\Delta\ell_{\text{step}} = 10^{-8}R_0$.

B Shell, membrane and droplet regime

In the following, we discuss numerical solutions of the shape equations for the general asymmetric case for three different types of interface elasticity: liquid lenses, lens-shaped capsules with a Hookean membrane (elastic lenses), and capsules with Hookean shell elasticity as shown in Fig. 4. We specify shape equations and the matching conditions for the three different regimes.

B.1 Liquid lens. The liquid lens is the simplest case discussed in this section, as it is obtained in the absence of any elastic tension, $Y_{2D} \approx 0$ ($\tau_s = \tau_\phi = \gamma$) and $E_B \approx 0$ ($q = 0$ and $m_s = m_\phi = 0$). For this liquid surface there is no reference shape, and surface tension and incompressibility determine the droplet shape. From the local force balance condition $p_0 dV = \sigma dA$, we obtain the Laplace–Young equation,

$$p_0 = \gamma(\kappa_s + \kappa_\phi), \tag{45}$$

which can be recast as a set of three shape equations

$$r'(s_0) = \cos\psi, \quad z'(s_0) = \sin\psi$$

$$\psi'(s_0) = p_0/\gamma - \sin\psi/r, \tag{46}$$

using cylindrical parametrization. This set of equations also directly derives from (5) by employing the limits given above. The resulting shapes have constant mean curvature according to the Laplace eqn (45) (or according to $\kappa_s + \kappa_\phi = \psi' + \sin\psi/r =$ const in (46)), which only allows lens shapes that are composed of two spherical caps with the same radius R.

For the numerical determination of the shape of the liquid lens we shoot from both apices with boundary conditions $r(0) = r(L_0) = 0$ and $\psi(0) = \pi - \psi(L_0) = 0$. We will determine two shooting parameters $z(0)$ and $z(L_0)$ such that $z^+(\ell) = z^-(\ell) = 0$. Because we have three shape eqn (45), there are no free shooting parameters left.

There are, however, three matching conditions at the AB-interface at $s_0 = \ell$: the Neumann triangle conditions (40) and (41) for force equilibrium in the z- and r-direction, respectively, which become ($q = 0$, $\tau_s^- = \tau_\phi^- = \gamma_A$, $\tau_s^+ = \tau_\phi^+ = \gamma_B$)

$$f_r \equiv \gamma_A \cos\psi^-(\ell) - \gamma_B \cos\psi^+(\ell) - \sigma = 0$$

$$f_z \equiv \gamma_A \sin\psi^-(\ell) - \gamma_B \sin\psi^+(\ell) = 0 \tag{47}$$

and the continuity condition $r^-(\ell) = r^+(\ell)$. As shown in Section A.2, this continuity equation is actually equivalent to the Neumann condition $f_z = 0$ for force equilibrium in the z-direction. For the liquid lens, there is no reference shape, and the matching conditions have to be used to determine the arc lengths $L_0 - \ell$ and ℓ of the upper and lower parts. We thus have two independent matching conditions for two unknown parameters ℓ and L_0. Numerically, we use the full overdetermined set of three matching conditions because we find that this leads to faster convergence of the shooting method. We note that liquid lenses exhibit a kink at the interface, *i.e.*, there is no continuity of ψ at the AB-interface. We also note that, because there is no elastic energy or reference shape, L_0 is not fixed beforehand by the reference shape and ℓ does not have to be determined from energy minimization as will be the case for Hookean membranes and shells.

B.2 Elastic lens. In the case of finite stretching resistance Y_{2D}, but vanishing bending rigidity $E_B \approx 0$, *i.e.*, vanishing shell thickness $H \approx 0$, we have an elastic lens with Hookean membrane elasticity with vanishing bending moments $m_s = m_\phi = 0$ and vanishing transverse shear stress $q = 0$.

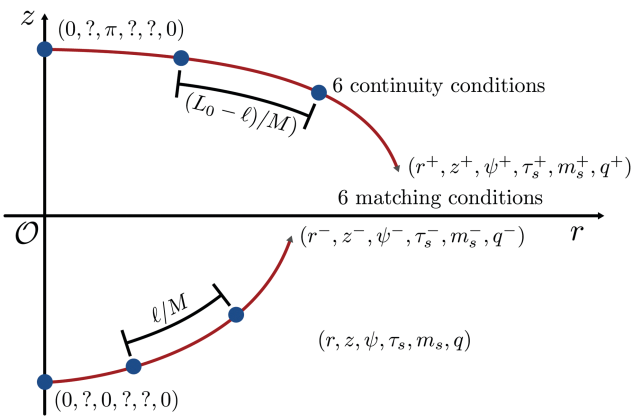

Fig. 9 Illustration of the multiple shooting method applied to numerically solve the shape equations. The r–z-plane is separated by a liquid–liquid interface at $z = 0$ arising from two different liquid phases A and B residing in the lower and upper half-spaces, respectively. The lower and upper branches are integrated from the apices on the z-axis to the interface on the r-axis, where we employ matching conditions corresponding to the different limit cases (Hookean membrane and Hookean shell) as discussed in this section.

The system (5) reduces to four coupled nonlinear differential equations

$$\begin{aligned} r'(s_0) &= \lambda_s \cos\psi, \quad z'(s_0) = \lambda_s \sin\psi, \\ \psi'(s_0) &= \lambda_s (p - \kappa_\phi \tau_\phi)/\tau_s, \\ \tau_s'(s_0) &= \lambda_s \left(\frac{\tau_\phi - \tau_s}{r} \cos\psi + p_s \right). \end{aligned} \tag{48}$$

Shapes are still similar to liquid lenses, and there is a kink at the AB-interface because there is no continuity of ψ.

For the numerical determination of the elastic lens shape we shoot from both apices with boundary conditions $r(0) = r(L_0) = 0$ and $\psi(0) = \pi - \psi(L_0) = 0$. The two shooting parameters $z(0)$ and $z(L_0)$ are determined from $z^+(\ell) = z^-(\ell) = 0$. Because we have four shape eqn (48), there are two free shooting parameters $\tau_s(0)$ and $\tau_s(L_0)$ left, which have to be determined from matching conditions at the AB-interface at $s_0 = \ell$.

As for a liquid lens, there are three matching conditions: the Neumann triangle conditions (40) and (41) for force equilibrium in the z- and r-direction, respectively, which become ($q = 0$)

$$\begin{aligned} f_r &\equiv \tau_s^-(\ell)\cos\psi^-(\ell) - \tau_s^+(\ell)\cos\psi^+(\ell) - \sigma = 0 \\ f_z &\equiv \tau_s^-(\ell)\sin\psi^-(\ell) - \tau_s^+(\ell)\sin\psi^+(\ell) = 0, \end{aligned} \tag{49}$$

and the continuity condition $r^-(\ell) = r^+(\ell)$. Again, this continuity equation is actually equivalent to the Neumann condition $f_z = 0$ for force equilibrium in the z-direction as shown in Section A.2. Two independent matching conditions can be used to determine the two shooting parameters $\tau_s(0)$ and $\tau_s(L_0)$. Again, we use the full over-determined set of three matching conditions, which leads to faster convergence of the shooting method. Finally, the arc length position ℓ of the AB-interface is determined by total energy minimization.

In the symmetric case, where $\gamma_A = \gamma_B$ and $\psi^-(\ell) = \pi - \psi^+(\ell)$, we find $\tau_s^-(\ell) = \tau_s^+(\ell)$. Note that the tensions τ_s^- and τ_s^+ include the liquid interface tensions γ_A and γ_B in addition to elastic contributions. In the symmetric case, the shooting parameters τ_s at the upper and lower apices are identical and thereby only one parameter is left. Symmetry with respect to the liquid–liquid interface also inherently satisfies the conditions $r^+(\ell) - r^-(\ell) = 0$ and $f_z = 0$ such that we are left with exactly one matching condition $f_r = 0$ from the Neumann condition (41) for force equilibrium in the r-direction.

Numerically calculated shapes of elastic lenses are shown in Fig. 4 both for tensile ($\sigma > 0$) and contractile ($\sigma < 0$) interfacial tensions.

B.3 Elastic shells. Finally, we incorporate the effect of a finite bending rigidity. Then we have the full set (5) of six shape equations. We shoot from both apices with boundary conditions $r(0) = r(L_0) = 0$, $\psi(0) = \pi - \psi(L_0) = 0$ and $q(0) = q(L_0) = 0$. The two shooting parameters $z(0)$ and $z(L_0)$ are determined from $z^+(\ell) = z^-(\ell) = 0$. Now we have four free shooting parameters $\tau_s(0)$, $\tau_s(L_0)$, $m_s(0)$, and $m_s(L_0)$ left, which have to be determined from matching conditions at the AB-interface at $s_0 = \ell$.

There are five matching conditions at the AB-interface: the continuity conditions $r^-(\ell) = r^+(\ell)$ and also $\psi^+(\ell) = \psi^-(\ell)$ (see eqn (33)) because kinks in the capsule shell are now suppressed by bending energy. Moreover, we also have the continuity condition $m_s^+(\ell) = m_s^-(\ell)$ (see eqn (42)) from the moment equilibrium at the AB-interface and two Neumann conditions (40) and (41) for force equilibrium in the z- and r-direction. The two Neumann conditions can be rearranged into direct jump conditions for τ_s and q at the AB-interface,

$$\begin{aligned} q^+(\ell) - q^-(\ell) &= \sigma \sin\psi^-(\ell) \\ \tau_s^+(\ell) - \tau_s^-(\ell) &= -\sigma \cos\psi^-(\ell). \end{aligned} \tag{50}$$

Again, one Neumann condition is actually equivalent to the continuity condition $r^-(\ell) = r^+(\ell)$ as shown in Section A.2, such that we have a set of four independent matching conditions for four shooting parameters. Numerically, we achieve faster convergence employing the over-determined set of all five matching conditions. The arc length position ℓ of the AB-interface is determined by total energy minimization.

Numerically calculated shapes for elastic shells are also shown in Fig. 4 both for tensile ($\sigma > 0$) and contractile ($\sigma < 0$) interfacial tensions.

C Analytical description of adsorbed shapes

As is evident from eqn (46) liquid lens shapes exhibit constant curvature and, thus, can be constructed from spherical caps. In this section, we use this fact to obtain an exact analytical result for the contact angle and the height of liquid lenses. We generalize this approach to elastic lenses by taking also elastic stresses into account and obtain an approximative theory, which gives the contact angle and the height of an elastic lens by solving numerically a single algebraic equation. Finally, these theoretical results enable a determination of Young's modulus of an elastic lens by a single measurement of the height or the contact angle. Furthermore, we give an approximative description of the rounding at the contact at finite bending rigidity, where the shapes are more discus- than lens-shaped, that is conceptually analogous to the Pogorelov approach to buckling.

C.1 Liquid lens. Lenticular liquid shapes have been discussed in the literature both at a liquid–liquid interface[57] and on a solid substrate,[58,59] and analytical solutions for liquid lenses at liquid–liquid interfaces can be obtained analogously. We restrict ourselves here to the symmetric case $\gamma \equiv \gamma_A = \gamma_B$. The total energy of the system is given by

$$E = \gamma A - \sigma A_B, \tag{51}$$

where A is the total area of the liquid lens and A_B the occupied cross-section area within the liquid–liquid interface plane. We use the fact that the liquid lens is composed of two spherical caps of equal radius $R = 2\gamma/p_0$ (for the symmetric case) according to the Laplace eqn (45), and of equal base radius R_B. Then $A = 2\pi(R^2 + h^2)$ is the surface of the lens (two spherical caps) and $A_B = \pi {R_B}^2$ the occupied cross-section area within the liquid–liquid interface plane. Here, h denotes the height of the spherical caps, which is related to R_B and R *via* ${R_B}^2 = 2Rh - h^2$, see also Fig. 10(B) for the involved quantities.

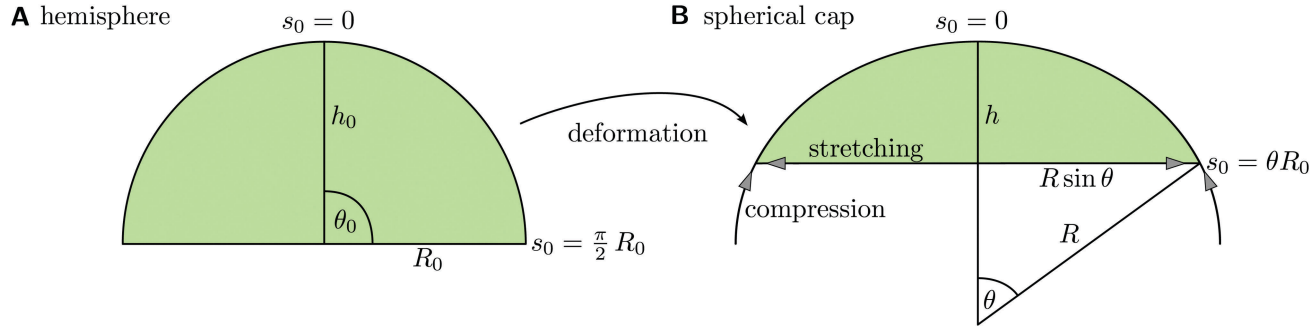

Fig. 10 Deforming a hemispherical rest shape (A) into a spherical cap (B). The resulting spherical cap has constant tension τ_s = const in the meridional direction, constant tension τ_ϕ = const in the circumferential direction, but tensions are anisotropic, *i.e.*, $\tau_s \neq \tau_\phi$ violating the force balance conditions (28) (i). We conclude that spherical caps with a hemispherical rest shape exhibit inhomogeneous stresses in order to fulfill (28) (i).

In the following, we measure lengths in units of the radius R_0 of a spherical droplet of the same volume $V \equiv 4\pi {R_0}^3/3$ and thereby introduce reduced quantities $\tilde{h} \equiv h/R_0$, $\tilde{R} \equiv R/R_0$, and $\tilde{V} \equiv V/{R_0}^3$. For a fixed volume,

$$\tilde{V} = \frac{\pi\tilde{h}}{3}\left(3\tilde{R} - \tilde{h}\right) = \frac{4\pi}{3} = \tilde{V}_0, \tag{52}$$

the radius R and the height h are related by

$$\tilde{R}(\tilde{h}) = \frac{1}{3}\left(\frac{2}{\tilde{h}^2} + \tilde{h}\right). \tag{53}$$

We can now write the energy (51) as a function of the reduced height $\tilde{h}$, minimize with respect to the reduced height $\tilde{h}$, and find the equilibrium height

$$\tilde{h} = \left(\frac{1 - \sigma/2\gamma}{1 + \sigma/4\gamma}\right)^{1/3} \tag{54}$$

as a function of σ/γ. We obtain the opening angle θ from the geometric relation

$$\cos\theta(\tilde{h}) = 1 - \frac{\tilde{h}}{\tilde{R}(\tilde{h})} \tag{55}$$

and, finally, the pressure from the Laplace–Young equation

$$p_0(\tilde{h}) = \frac{2\gamma}{\tilde{R}(\tilde{h})} = \frac{6\tilde{h}^2\gamma}{2 + \tilde{h}^3}. \tag{56}$$

If we use $\tilde{h}$ as a function of σ/γ from eqn (54) in these relations we find θ and p_0 as a function of σ/γ.

The result (54) for $\tilde{h}$ as a function of σ/γ can likewise be obtained by starting from the Neumann condition $f_r = 0$ in (47), employing the geometric relation (55) and the volume constraint (53),

$$\sigma = 2\gamma\cos\theta(\tilde{h}) = 2\gamma\left(1 - \frac{\tilde{h}}{\tilde{R}(\tilde{h})}\right) = 4\gamma\frac{1 - \tilde{h}^3}{2 + \tilde{h}^3} \tag{57}$$

(for $\theta = \psi^-(\ell) = \pi - \psi^+(\ell)$ and $\gamma = \gamma_A = \gamma_B$). Solving for $\tilde{h}$ gives (54).

C.2 Elastic lens. For the symmetric case, we can derive an approximative analytical solution for the elastic membrane shape based on a spherical cap approximation. We investigate partially spherical solutions, because, intuitively, the difference between a liquid droplet and a liquid droplet coated with an elastic membrane should be negligible for small interface loads as also suggested by the numerically calculated shapes of elastic lenses. Force balance for an unloaded spherical cap implies a constant tension τ_s = const[53] such that, additionally, $\tau_s = \tau_\phi$ must hold to fulfill the force balance conditions (28) (i).

Deforming a hemisphere into a spherical cap by uniform strains leads, however, to anisotropic tensions $\tau_s \neq \tau_\phi$. The spherical cap has only one free parameter, which is its reduced height $\tilde{h}$, as has already been introduced above in the context of liquid lenses. From geometrical arguments (see Fig. 10) we can calculate the uniform stretches λ_s and λ_ϕ for the deformation into a spherical cap,

$$\lambda_s = \frac{2\theta(\tilde{h})}{\pi}\tilde{R}(\tilde{h}) \quad \text{and } \lambda_\phi = \tilde{R}_B = \tilde{R}(\tilde{h})\sin(\theta(\tilde{h})), \tag{58}$$

where $\tilde{R}(\tilde{h})$ is the reduced radius as given by the volume constraint (53) and $\theta(\tilde{h})$ is the opening angle of the spherical caps according to (55). Obviously $\lambda_s < \lambda_\phi$ because $\theta < \pi/2$ and $R > R\sin\theta$, *i.e.*, the stretches (13) are anisotropic. Inserting these stretches into the constitutive relations (4) we also obtain anisotropic stresses, $\tau_s < \tau_\phi$. Therefore, assuming constant tensions in a spherical cap formed from a hemispherical rest shape violates the force balance conditions (28). For $\gamma \geq Y_{2D}$, *i.e.*, small deviations from the fluid-like behavior, deviations from force balance are also small, and we can use spherical caps as an approximation.

Inserting the uniform strains (13) into the constitutive relations (4) gives the stresses $\tau_s(\tilde{h})$ and $\tau_\phi(\tilde{h})$ as a function of the reduced spherical cap height $\tilde{h}$. Then we employ the Neumann condition $f_r = 0$ from eqn (49) in the symmetric case, *i.e.*, $\theta = \psi^-(\ell) = \pi - \psi^+(\ell)$ and $\gamma = \gamma_A = \gamma_B$, the geometric relation (55) and the volume constraint (53), to obtain

$$\sigma = 2\tau_s(\tilde{h})\cos\theta(\tilde{h}) = 2\tau_s(\tilde{h})\left(1 - \frac{\tilde{h}}{\tilde{R}(\tilde{h})}\right) = 4\tau_s(\tilde{h})\frac{1 - \tilde{h}^3}{2 + \tilde{h}^3} \tag{59}$$

analogously to eqn (57). Solving this equation for $\tilde{h}$ gives the height as a function of σ/γ and γ/Y_{2D}. In the fluid regime $\gamma \gg Y_{2D}$ ($\tilde{\gamma} \gg 1$ in Fig. 5(A and B)), we have $\tau_s(\tilde{h}) \approx \gamma$ and find $\cos\theta \approx 2(1 - \tilde{h}) \sim \sigma/\gamma$ for small σ/γ. In the elastic regime $\gamma \ll Y_{2D}$ ($\tilde{\gamma} \ll 1$ in Fig. 5(A and B)), we have $\tau_s(\tilde{h}) \sim Y_{2D}(1 - \tilde{h})^2$,

which gives $\cos\theta \approx 2(1-\tilde{h}) \sim (\sigma/Y_{2D})^{1/3}$ for small σ/Y_{2D}. From the Laplace–Young equation (third eqn (48)), we then find the pressure p_0 as a function of h,

$$p_0(\tilde{h}) = \frac{3\tilde{h}^2(\tau_s(\tilde{h}) + \tau_\phi(\tilde{h}))}{2+\tilde{h}^3}, \tag{60}$$

and, thus, as a function of σ/γ and γ/Y_{2D}.

Note that instead of solving (59), we could likewise minimize the free energy for the elastic lens, which is obtained analogously to (51), but with an additional elastic energy term as in (3).

C.3 Pogorelov approximation for finite E_B. For $E_B > 0$ the edge of the elastic lens becomes rounded as shown in Fig. 11(A). The curvature κ_s at the AB-interface is a characteristic geometric feature of these shapes, which depends on the elastic properties of the capsule and the interface load. In Fig. 5(C), we found a scaling $\kappa_s \sim E_B^{-1/2}$ for the curvature κ_s from numerical simulations. We can derive this scaling from an adaption of Pogorelov's theory[52] as has been used in ref. 60 and 61. The reader is referred to Fig. 11(B) for the involved geometric quantities. We start from an elastic lens shape for vanishing bending rigidity $E_B \approx 0$, which is described by the contour $(r(s_0), z(s_0))$ and has a sharp edge at the AB-interface. If the bending rigidity is introduced, the shape becomes rounded at the edge, which is described by an additional displacement field $(v(s_0), u(s_0))$ such that

$$(r(s_0), z(s_0)) \to (r(s_0) + v(s_0), z(s_0) + u(s_0)). \tag{61}$$

during rounding. Rounding involves two additional energies contributing to the shape: the additional bending energy U_B associated with the bending rigidity and an additional mechanical work U_σ performed against the surface tension σ because rounding displaces the three phase contact line against the surface tension σ.

Since the interface load acts in the radial direction, it is reasonable to assume that $u(s_0) = 0$, *i.e.*, only radial shape perturbations occur. This allows us to write the total energy change, induced by bending and pulling against σ while starting at the elastic lens, as

$$U = U_B + U_\sigma = 2\int_\ell^{\ell+\varepsilon} \mathrm{d}s_0 \left[\pi R_D E_B v''(s_0)^2 - \pi R_D \sigma v(s_0)\delta(s_0-\ell)\right] \tag{62}$$

where ε describes a small arc length region over which the kink of the shape is rounded and R_D is the radius of the circle in the interface plane, *i.e.*, the radius of the interface cross-section. In eqn (62) we neglect the apparent hoop stretching as well as higher order and constant terms of the bending energy (for a detailed analysis, see ref. 52). Throughout the following calculations we use approximations for small α, which is the turning angle of the shape at the AB-interface and related to the opening angle of the elastic lens *via* $\alpha = \pi/2 - \theta$. To find the corresponding characteristic arc length scale $\xi \sim \alpha\kappa_s^{-1}$ on which the shape gets bent at the interface, we non-dimensionalize eqn (62) according to

$$\begin{aligned} s_0 &= \xi\bar{s}_0, \quad -v(s_0) = \xi\alpha\bar{v}(\bar{s}_0), \\ -v''(s_0) &= \frac{\mathrm{d}^2 v(s_0)}{\mathrm{d}s_0^2} = \alpha\frac{\xi \mathrm{d}^2\bar{v}(\bar{s}_0)}{\xi^2 \mathrm{d}\bar{s}_0^2} = \frac{\alpha}{\xi}\bar{v}(\bar{s}_0)'', \end{aligned} \tag{63}$$

and recast the energies in (62) as

$$U_B = E_B R_D \frac{\alpha^2}{\xi}\int_{\bar{\ell}}^{\bar{\ell}+\bar{\varepsilon}} \mathrm{d}\bar{s}_0 \bar{v}(\bar{s}_0)''^2, \tag{64}$$

$$U_\sigma = \pi R_D \sigma \xi \alpha \int_{\bar{\ell}}^{\bar{\ell}+\bar{\varepsilon}} \mathrm{d}\bar{s}_0 \bar{v}(\bar{s}_0)\delta(\bar{s}_0 - \bar{\ell}). \tag{65}$$

Minimizing the total energy $U = U_B + U_\sigma$ with respect to ξ we find the scaling relations

$$\xi \sim \alpha^{1/2}\sqrt{\frac{E_B}{\sigma}}, \quad U = U_0 \sim R_D \alpha^{3/2}\sqrt{E_B\sigma}. \tag{66}$$

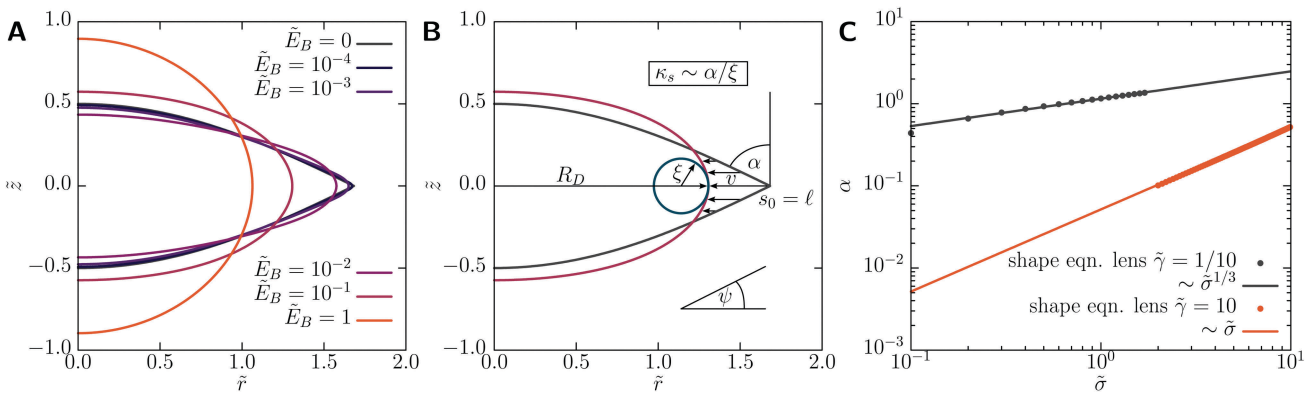

Fig. 11 (A) Shapes with increasing bending modulus. The bending modulus of the shell's material determines the curvature at the liquid–liquid interface at $z = 0$ where the interface load σ pulls the equator outwards. Increasing the bending modulus increases the radius of curvature at the interface. Shapes were calculated in the elastic regime with $\gamma/Y_{2D} = 1/10$. (B) Illustration of the geometrical quantities employed within the Pogorelov approximation. We assume that the major contribution to the bending energy is located within a small region of size ξ at $s_0 = \ell$, *i.e.*, the liquid–liquid interface. When the bending energy is switched on, the kink of the elastic lens vanishes and the contact angle α decreases from a finite value to zero. This deformation is quantified by the radial displacement field $v(s_0)$. The curvature at the interface is accessible *via* $\kappa_s \sim \alpha/\xi$ employing the length scale ξ and the contact angle α. (C) Numerical verification of the scaling of the contact angle, see eqn (67).

The dimensionless integrals in eqn (65) only contribute numerical prefactors; the essential result is the scaling behavior of U_0 and ξ. Note that the above scaling relations still depend on α. This dependence can be eliminated by employing the symmetric Neumann force balance condition (59), $\sigma = 2\tau_s(\tilde{h})\sin\alpha$ and the geometric relation $\sin\alpha = 2(1-\tilde{h}^3)(2+\tilde{h}^3)$. In the fluid regime $\gamma \gg Y_{2D}$, we have $\tau_s(\tilde{h}) \approx \gamma$ and find $\sin\alpha \sim \sigma/2\gamma$. In the elastic regime $\gamma \ll Y_{2D}$, we have $\tau_s(\tilde{h}) \sim Y_{2D}(1-\tilde{h})^2 \sim Y_{2D}\sin^2\alpha$ for small α. For small α, this leads to

$$\alpha \sim \begin{cases} (\sigma/Y_{2D})^{1/3}, & \gamma \ll Y_{2D} \quad \text{(elastic)} \\ \sigma/\gamma, & \gamma \gg Y_{2D} \quad \text{(fluid)}, \end{cases} \tag{67}$$

in the two regimes. The above scaling behavior of α is verified numerically in Fig. 11(C), where we measured α for an elastic lens dependent on σ/Y_{2D} for two different values of γ corresponding to the elastic respectively fluid regime. Inserting these scaling relations into eqn (66) gives

$$\xi \sim \begin{cases} E_B^{1/2}\sigma^{-1/3}Y_{2D}^{-1/6}, & \gamma \ll Y_{2D} \quad \text{(elastic)} \\ E_B^{1/2}\gamma^{-1/2}. & \gamma \gg Y_{2D} \quad \text{(fluid)}. \end{cases} \tag{68}$$

From $\kappa_s \sim \alpha/\xi$ we finally obtain the scaling laws for the shell's curvature at the AB-interface

$$\kappa_s \sim \begin{cases} E_B^{-1/2}\sigma^{2/3}Y_{2D}^{-1/6}, & \gamma \ll Y_{2D} \quad \text{(elastic)} \\ E_B^{-1/2}\sigma\gamma^{-1/2}, & \gamma \gg Y_{2D} \quad \text{(fluid)}. \end{cases} \tag{69}$$

The dependence on the bending modulus, $\kappa_s \propto E_B^{-1/2}$, is universal, *i.e.*, independent of whether we are in the fluid or elastic regime. For comparison, spherical shells which buckle upon deflation have $\kappa_s \propto E_B^{-1/4}$ at the spherical rim of the indentation.[60,61]

Acknowledgements

We acknowledge financial support by the Deutsche Forschungsgemeinschaft *via* SPP 1726 "Microswimmers" (KI 662/7-1).

References

1 M. Vert, K.-H. Hellwich, M. Hess, P. Hodge, P. Kubisa, M. Rinaudo and F. Schué, *et al.*, *Pure Appl. Chem.*, 2012, **84**, 377–410.
2 A. Dinsmore, M. F. Hsu, M. Nikolaides, M. Marquez, A. Bausch and D. Weitz, *Science*, 2002, **298**, 1006–1009.
3 E. Donath, G. B. Sukhorukov, F. Caruso, S. A. Davis and H. Möhwald, *Angew. Chem., Int. Ed.*, 1998, **37**, 2201–2205.
4 L. J. De Cock, S. De Koker, B. G. De Geest, J. Grooten, C. Vervaet, J. P. Remon, G. B. Sukhorukov and M. N. Antipina, *Angew. Chem., Int. Ed.*, 2010, **49**, 6954–6973.
5 G. Orive, R. M. Hernández, A. R. Gascón, R. Calafiore, T. M. S. Chang, P. de Vos, G. Hortelano, D. Hunkeler, I. Lacík and J. L. Pedraz, *Trends Biotechnol.*, 2004, **22**, 87–92.
6 M. T. Cook, G. Tzortzis, D. Charalampopoulos and V. V. Khutoryanskiy, *J. Controlled Release*, 2012, **162**, 56–67.
7 S. Mondal, *Appl. Therm. Eng.*, 2008, **28**, 1536–1550.
8 I. M. Martins, M. F. Barreiro, M. Coelho and A. E. Rodrigues, *Chem. Eng. J.*, 2014, **245**, 191–200.
9 B. Assa, D. Therriault, E. Haddad and W. Jamroz, *Adv. Mater. Sci. Eng.*, 2012, 854203.
10 S. R. White, N. Sottos, P. Geubelle, J. Moore, M. Kessler, S. Sriram, E. Brown and S. Viswanathan, *Nature*, 2001, **409**, 794–797.
11 A. Gharsallaoui, G. Roudaut, O. Chambin, A. Voilley and R. Saurel, *Food Res. Int.*, 2007, **40**, 1107–1121.
12 M. Buenemann and P. Lenz, *Phys. Rev. E: Stat., Nonlinear, Soft Matter Phys.*, 2008, **78**, 051924.
13 H. N. Yow and A. F. Routh, *Soft Matter*, 2006, **2**, 940–949.
14 K. L. Thompson, M. Williams and S. P. Armes, *J. Colloid Interface Sci.*, 2015, **447**, 217–228.
15 H. Rehage, M. Husmann and A. Walter, *Rheol. Acta*, 2002, **41**, 292–306.
16 L. Vaccari, D. B. Allan, N. Sharifi-Mood, A. R. Singh, R. L. Leheny and K. J. Stebe, *Soft Matter*, 2015, **11**, 6062–6074.
17 K. Xie, C. de Loubens, F. Dubreuil, D. Z. Gunes, M. Jaeger and M. Léonetti, *Soft Matter*, 2017, **13**, 6208–6217.
18 J. Hu, H.-Q. Chen and Z. Zhang, *Mater. Chem. Phys.*, 2009, **118**, 63–70.
19 O. I. Vinogradova, O. V. Lebedeva and B.-S. Kim, *Annu. Rev. Mater. Res.*, 2006, **36**, 143–178.
20 M. P. Neubauer, M. Poehlmann and A. Fery, *Adv. Colloid Interface Sci.*, 2014, **207**, 65–80.
21 H. Kusumaatmaja and R. Lipowsky, *Soft Matter*, 2011, **7**, 6914.
22 F. Jülicher and R. Lipowsky, *Phys. Rev. E: Stat. Phys., Plasmas, Fluids, Relat. Interdiscip. Top.*, 1996, **53**, 2670.
23 A. Zumdieck, K. Kruse, H. Bringmann, A. A. Hyman and F. Jülicher, *PLoS One*, 2007, **2**, e696.
24 B. J. Park, T. Brugarolas and D. Lee, *Soft Matter*, 2011, **7**, 6413–6417.
25 B. J. Park and D. Lee, *Soft Matter*, 2012, **8**, 7690–7698.
26 W. Richtering, *Langmuir*, 2012, **28**, 17218–17229.
27 H. Mehrabian, J. Harting and J. H. Snoeijer, *Soft Matter*, 2016, **12**, 1062–1073.
28 K. Geisel, A. A. Rudov, I. I. Potemkin and W. Richtering, *Langmuir*, 2015, **31**, 13145–13154.
29 R. W. Style, L. Isa and E. R. Dufresne, *Soft Matter*, 2015, **11**, 7412–7419.
30 A. Rauh, M. Rey, L. Barbera, M. Zanini, M. Karg and L. Isa, *Soft Matter*, 2017, **13**, 158–169.
31 S. Knoche and J. Kierfeld, *Langmuir*, 2015, **31**, 5364–5376.
32 S. Knoche, D. Vella, E. Aumaitre, P. Degen, H. Rehage, P. Cicuta and J. Kierfeld, *Langmuir*, 2013, **29**, 12463–12471.
33 M. Nagel, T. A. Tervoort and J. Vermant, *Adv. Colloid Interface Sci.*, 2017, 1–19.
34 J. Hegemann, S. Knoche, S. Egger, M. Kott, S. Demand, A. Unverfehrt, H. Rehage and J. Kierfeld, *J. Colloid Interface Sci.*, 2018, **513**, 549–565.
35 S. Knoche and J. Kierfeld, *Phys. Rev. E: Stat., Nonlinear, Soft Matter Phys.*, 2011, **84**, 046608.
36 S. Knoche and J. Kierfeld, *Soft Matter*, 2014, **10**, 8358–8369.
37 K. S. Chang and W. L. Olbricht, *J. Fluid Mech.*, 1993, **250**, 609–633.

38 C. de Loubens, J. Deschamps, F. Edwards-Levy and M. Leonetti, *J. Fluid Mech.*, 2016, **789**, 750–767.
39 C. de Loubens, J. Deschamps, M. Georgelin, A. Charrier, F. Edwards-Levy and M. Leonetti, *Soft Matter*, 2014, **10**, 4561.
40 G. Pieper, H. Rehage and D. Barthès-Biesel, *J. Colloid Interface Sci.*, 1998, **202**, 293–300.
41 H.-H. Boltz and J. Kierfeld, *Phys. Rev. E: Stat., Nonlinear, Soft Matter Phys.*, 2015, **92**, 033003.
42 H.-H. Boltz and J. Kierfeld, *Eur. Phys. J.: Spec. Top.*, 2016, **225**, 2269–2285.
43 A. Libai and J. G. Simmonds, *The Nonlinear Theory of Elastic Shells*, Cambridge University Press, 1998.
44 D. Vella, *Annu. Rev. Fluid Mech.*, 2015, **47**, 115–135.
45 M. P. Do Carmo, *Differential Forms and Applications*, Springer, 1994, pp. 77–98.
46 P. Ciarlet, *An Introduction to Differential Geometry with Applications to Elasticity*, Springer, Netherlands, 2006.
47 E. Efrati, E. Sharon and R. Kupferman, *J. Mech. Phys. Solids*, 2009, **57**, 762–775.
48 D. Barthès-Biesel, A. Diaz and E. Dhenin, *J. Fluid Mech.*, 2002, **460**, 211–222.
49 F. E. Neumann, *Vorlesungen über mathematische Physik: Vorlesungen über die Theorie der Capillarität*, BG Teubner, 1894, vol. 7.
50 J. B. Keller, *Phys. Fluids*, 1998, **10**, 3009–3010.
51 R. Finn, *Equilibrium Capillary Surfaces*, Springer, 1986.
52 A. V. Pogorelov, *Bendings of surfaces and stability of shells*, American Mathematical Soc., 1988, vol. 72.
53 L. D. Landau and E. M. Lifschitz, *Theory of Elasticity*, Pergamon Press, Oxford, 1970.
54 U. Seifert and R. Lipowsky, *Phys. Rev. A: At., Mol., Opt. Phys.*, 1990, **42**, 4768–4771.
55 F. Bresme and M. Oettel, *J. Phys.: Condens. Matter*, 2007, **19**, 413101.
56 J. Jose, M. Kamp, A. van Blaaderen and A. Imhof, *Langmuir*, 2014, **30**, 2385–2393.
57 H. M. Princen, *J. Colloid Sci.*, 1963, **18**, 178–195.
58 B. Widom, *J. Phys. Chem.*, 1995, **99**, 2803–2806.
59 P. Blecua, R. Lipowsky and J. Kierfeld, *Langmuir*, 2006, **22**, 11041–11059.
60 S. Knoche and J. Kierfeld, *EPL*, 2014, **106**, 24004.
61 S. Knoche and J. Kierfeld, *Eur. Phys. J. E: Soft Matter Biol. Phys.*, 2014, **37**, 62.